FLOW-THROUGH MICROFLUIDIC DEVICE FOR HIGH-EFFICIENCY TRANSFECTION OF MAMMALIAN CELLS THROUGH COMBINED MICROELECTROPORATION AND SONOPORATION

A Thesis

by

WHITNEY LEIGH LONGSINE

Submitted to the Office of Graduate Studies of
Texas A&M University
in partial fulfillment of the requirements for the degree of

MASTER OF SCIENCE

May 2011

Major Subject: Electrical Engineering

Flow-through Microfluidic Device for High-efficiency Transfection of Mammalian Cells through Combined Microelectroporation and Sonoporation

FLOW-THROUGH MICROFLUIDIC DEVICE FOR HIGH-EFFICIENCY TRANSFECTION OF MAMMALIAN CELLS THROUGH COMBINED MICROELECTROPORATION AND SONOPORATION

A Thesis

by

WHITNEY LEIGH LONGSINE

Submitted to the Office of Graduate Studies of
Texas A&M University
in partial fulfillment of the requirements for the degree of

MASTER OF SCIENCE

Approved by:

Chair of Committee,	Arum Han
Committee Members,	Jun Kameoka
	Michael McShane
	Raffaella Righetti
Head of Department,	Costas Georghiades

May 2011

Major Subject: Electrical Engineering

ABSTRACT

Flow-through Microfluidic Device for High-efficiency Transfection of Mammalian Cells through Combined Microelectroporation and Sonoporation. (May 2011)

Whitney Leigh Longsine, B.S., Texas A&M University

Chair of Advisory Committee: Dr. Arum Han

In this study we are presenting a proof-of-concept microfluidic device that simultaneously applies the conditions required for microelectroporation and micro-sonoporation in a flow-through fashion that allows for high throughput, high efficiency transfection of mammalian cells. During the design stage, we developed a low-cost, high-resolution polymer microfabrication technique termed laser stenciling. While few other electro-sonoporation protocols have been reported, to the best of our knowledge, we are the first to incorporate microelectroporation, which has been well established in literature to be advantageous to conventional electroporation, with flow-through micro-sonoporation. When comparing transfection efficiency for our electro-sonoporation method to that of sonoporation or microelectroporation alone, we observed single batch improvements up to 20% and 17%, respectively. The average improvement in efficiency was approximately 15% greater than achieved with sonoporation and 10% greater than that of electroporation. Importantly, there was little difference in short term cell viability between the three methods (maintained at > 90%). The average transfection efficiency for electro-sonoporation was 81.25% and cell viability was 91.56%. Overall, we have presented a device and electro-sonoporation method that meets or outperforms the transfection efficiency and cell viability standards for HeLa cells set by other reported electroporation and sonoporation methods.

ACKNOWLEDGEMENTS

I would like to thank my advisor and committee chair, Dr. Arum Han, and my committee members, Dr. Righetti, Dr. McShane, and Dr. Kameoka, for their support in this work.

I would also like to thank Chiwan Koo, Han Wang, and Dr. Jeongyun Kim for all their help and assistance in accomplishing this research.

Finally, I would like to thank my husband for all his love and support, in myriad ways, and my parents and sister, who have always been instrumental in my personal success.

TABLE OF CONTENTS

Page

LIST OF FIGURES

LIST OF TABLES

1. INTRODUCTION AND LITERATURE REVIEW

1.1 Cell Transfection

The cell membrane acts as an effective barrier between the cytoplasm and contents within and the extracellular environment. It is impermeable to most substances and thus, the vast majority of a cell's biologically active structures are isolated from exterior manipulation. [1-2] Several methods have been developed to make the membrane temporarily permeable for the introduction of foreign substances into cells. The introduction of genetic materials and constructs is of particular interest for applications in gene therapy and genetic engineering and this process is commonly referred to as transfection.[2-3]

Example transfection methods include viral vector methods, where viruses act as carriers of genetic materials; chemical-based methods, which include the use of calcium phosphate and liposome-membrane fusion; physical methods, like particle bombardment (gene gun), fine-needle injection, and methods that create transient pores in the cell membrane, such as electroporation, and sonoporation.[4] Viral vector methods are highly efficient, but there are potential complications such as mutagenesis and inherent risks with inciting an immune response. Chemical-based methods have limited efficiency and physical methods like bombardment and injection are not selective and may disrupt cell function.[4]

Both electroporation and sonoporation methods have been demonstrated in temporarily permeabilizing the cell membrane to allow for foreign materials such as dyes, drugs, DNA, and proteins to transverse into the cytoplasm.

This thesis follows the style of *Lab on a Chip.*

1.2 Conventional Electroporation

Electroporation is the use of an externally applied electric field to form transient pores in the cell membrane and has been used to deliver genes and drugs into cells both *in vitro* and *in vivo*.[4-6] High electric fields, typically 1 – 10 kV/cm, are required to break down the dielectric layer over the cell membrane. Pore formation occurs when the transmembrane potential is greater than the breakdown voltage of the membrane, which is between 0.2 – 1.5 V. [1, 4] These nanometer-sized pores are transmembrane structures that are thought to be created by localized structural rearrangement of the cell membrane.[7-8] Permeabilization is reversible as long as the electric field exposure does not compromise the viability of the cells. Once the pores are created, materials within the extracellular environment can migrate into the cells.

A conventional electroporator is a bench-top device that consists of a pulsed power supply and a cuvette for loading the cells and materials to be transfected. The fixed-volume cuvette has two plate electrodes on its sides for connection to the power supply. The cell suspension is pipetted into the cuvette, which is then inserted into the electroporator. The electroporation parameters (voltage, capacitance, pulse length) can be set and adjusted on the instrument based on the cell type used. Pulse durations are typically on the order of a few μs to several ms.[8] Advantages of the bench-top electroporator include relatively rapid and straight-forward processing and the capability to treat large cell populations at once.[9] However, disadvantages include the risks and cost associated with the high voltage required, a rising ambient temperature that reduces cell viability, and limited transfection efficiency caused by a non-uniform electric field; higher electric fields that increase transfection in some cells can also cause irreversible electroporation and cell death in others.[3-4, 6, 9-10]

1.3 Microchip Electroporation

In recent years, several microchip electroporation devices have been presented by various groups. The primary motivations for those studies are the limitations and problems common with conventional electroporators. Namely, cells experience a non-uniform and unstable electric field inside the cuvette, which makes efficiency low. This electric field profile is unavoidable due to the large cuvette size and short pulse period.[11] The result is some cells are not exposed to an adequate electric field pulse and electroporation does not occur, while other cells are overexposed and destroyed. Furthermore, there are issues with elevated temperatures during the process, which can contribute to cell death. Also, the low-cost aluminum electrodes commonly used in commercial devices can produce Al^{3+} ions in the media, which causes unpredictable results.[6, 11-12] Finally, the cuvette size and corresponding spacing of electrodes requires operation of the instrument at several hundred volts, so extreme caution must be taken.

Micro-electroporators can overcome these issues and provide further improvements in device operation and results. A primary advantage seen in miniaturization is high efficiency transfection coupled with a substantial improvement in cell viability.[6] In microscale devices, high electric fields can be induced by placing electrodes in close proximity or by creating a constriction between the electrodes that focuses the electric field.[8, 13] Uniform electric fields can be achieved with a simple pulsed or AC voltage source, or in some cases a DC source, which can successfully generate the required electric field for electroporation. Based on the distance between the electrodes or built in constrictions and the proximity of the cells to the electrodes, supply voltages of 0.1 – 20 V have been demonstrated to produce the necessary field strength for permeabilization.[8, 11-12] This significant reduction in applied voltage provides

far less risk to the operator and also helps to diminish heating issues, which may improve the survival rate after treatment.[4, 8] In micro-electroporators, there is minimal heat generation due to low power consumption and rapid heat dissipation due to large surface area-to-volume ratios, and flow-through devices further minimize any potential local heating issues.[4, 8, 10, 14] Other advantages of microscale electroporation are reduced reagent consumption, the potential for integration with other microfluidic devices, and the capability for mass scale production.[6, 10]

At this point, many groups have developed and demonstrated micro-electroporation chips and a large portion of them have focused on either single-cell manipulation or flow-through devices. Advantages of single-cell electroporation include ensured exposure of individual cells to the electric field through trapping mechanisms resulting in very high transfection rates and the capability to incorporate the cell into an electrical circuit so that current through the cell can be monitored, which is a direct indicator of poration. Huang and Rubinsky presented an optically transparent microelectroporation device that incorporated individual cells in the chip's circuit, trapped by means of a pressure difference, where successful poration was measured by jumps in current indicative of drops in cell resistance.[9, 15] The work was extended by employing microfluidic channels to handle the cells in a flow-through manner, where they are transported to the electroporation site and permeabilized one-by-one.[2] Khine et al. demonstrated a parallel single cell electroporation device that sequestered individual cells in lateral trapping sites in PDMS channels and also monitored current as an indicator of electroporation.[1] This system was further scaled up to a 96-well format and developed into a bench-top type system with feedback control.[16] Valero et al. reported a single cell electroporation device that trapped cells in a flow channel at sites

with individually addressable electrodes and visually monitored the uptake of fluorescent dye and green fluorescent protein (GFP) to assess permeabilization.[17]

Advantages of flow-through devices without cell trapping include high throughput experiments as eliminating single-cell traps greatly reduces the time to process large batches of cells, a constant flow of solution that produces a cooling effect for the electrodes, and the capability to easily incorporate with additional microfluidic systems. Lin et al. developed a flow-type electroporation microchip comprised of sandwiched PMMA layers with electrodes positioned at the top and bottom of the flow channel. A continuous stream of cells were pumped through the device and exposed to a specific number of pulses as determined by the syringe pump flow rate.[4] Choi et al. presented a three-dimensional electrode structure that used dielectrophoresis for cell positioning within the flow channel prior to electroporation to ensure each cell was exposed to a uniform electric field.[10] Wang et al. developed a device with a serpentine structure micromilled in an Al bar on a plastic chip, which served as both the flow channel sidewalls and electroporation electrodes.[18] Wang and Lu reported a device that utilized geometric variation, where electroporation happened only in a defined segment of a microfluidic channel due to local DC field amplification in the single narrow section.[5] This work was further expanded to investigate multiple narrow sections to administer multiple pulses, which improved transfection yield.[13] Ziv et al. presented a similar narrow segment flow channel, but used AC electrical pulses (instead of DC) to overcome a gas bubble formation problem caused by electrolysis.[7] Kim et al. utilized polyelectrolytic salt bridges as ionic conductors to effectively separate the electrodes from the cell solution, eliminating bubble generation, heating shock, and chemical contamination while operating under a low DC voltage.[11] Both Guignet and Meyer and

Zhan et al. designed devices that performed droplet-based electroporation, the former with cell-containing droplets suspended between 96 electrode pairs by surface tension and ejected into 96-well plates post-treatment, and the latter with cells encapsulated in aqueous droplets in oil that were exposed to a single electrode pair along the flow channel.[19-20] Lin et al. developed an electroporation microchip that used an electrostatic force to attract plasmid DNA to the cell surfaces prior to electroporation to enhance transfection efficiency.[3] Similarly, Li et al. utilized magnetic fields to position DNA associated with magnetic nanoparticles near cell surfaces for enhanced gene transfection.[21]

1.4 Conventional Sonoporation

Sonoporation is the use of ultrasound waves to create transient permeability in cell membranes and, like electroporation, is effective both *in vitro* and *in vivo*.[22] It is non-invasive and can be focused, which is a great advantage *in vivo* as it allows for deep or shallow penetration to specific locations in the human body.[23] Acoustic cavitation is believed to be the primary mechanism for cell membrane disruption, and relies on dissolved air and/or solution impurities for cavitation nuclei.[22-23] Cavitation can be enhanced by the introduction of microbubbles, which greatly increase the amount of nuclei and reduce the cavitation threshold.[23] Furthermore, microbubbles, otherwise known as ultrasound contrast agents (UCA), can aid in the delivery of larger molecules. Commercially available UCAs, such as Optison®, are commonly used for this purpose. Similar to electroporation, the membrane permeabilization that occurs is not permanent, but cell viability is a concern at high exposure doses.[24] It is important to note that cell damage and death is typically far less extensive than with electroporation. Bench-top

sonoporators are commercially available, but generally sonoporation is performed with a general purpose piezoelectric transducer connected to an amplifier and function generator. Typically, the experiments are housed within a water bath (37°C) and the transducer is mounted a distance approximately equal to its focal length from the cell sample. Commonly used frequencies are in the range of 20 kHz to 7.5 MHz and both focused and unfocused and low and high amplitude fields have been employed.[23] Transfection efficiency is dependent upon acoustic pressure or energy, pulse length, duty cycle, repetition rate, exposure duration, cell concentration, and the properties of microbubbles, if utilized.[22-24]

Several groups have reported successful sonoporation *in vitro*, but the efficiencies and viabilities of cells post-procedure vary widely.[25] Zarnitsyn et al. sought to optimize transfection through adjusting various physical and acoustic parameters. Two previously reported transducer setups were compared, one operating at 500 kHz with the presence of Optison®[26] and the other operating at 24 kHz without any UCA.[27] They adjusted acoustic energy, cell concentration, and sonication temperature and from these configurations, the optimal condition was determined and showed to increase transfection by almost 100-fold relative to non-sonicated controls.[22] Taniyama et al. used Optison® microbubbles as carriers of plasmid DNA both *in vitro* and *in vivo*, using a conductivity gel based configuration rather than the more commonly used immersion style setup.[28] Koch et al. used ultrasound with the UCA Levovist® to enhance liposome-mediated gene transfer and expression in brain tumor cells.[29] Sonoporation efficiency has been reported to be significantly higher in the presence of a standing wave[23, 29], as emphasized by Kinoshita et al.[25] When the standing wave was essentially eliminated from the immersion-style setup, sonoporation was negligible. Furthermore,

the fashion of cell culture was investigated, showing that sonoporation efficiency was comparable in exposed suspensions and monolayers, but that viability was much higher in cell monolayers.[25]

There has been evidence to suggest that the cell membrane effects referred to as sonoporation may actually be a form of membrane wounding rather than the formation of pores (as in electroporation). Schlicher et al. report that membrane resealing time is more consistent with mechanical wounding, where portions of the membrane up to microns in size may be removed, and the subsequent healing is an active process involving trafficking intracellular vesicles to the site of injury, requires the presence of Ca^{2+}, and takes on the order of minutes.[30] On the other hand, Deng et al. used a voltage clamp technique to measure the real-time transmembrane current of a single *Xenopus oocyte* during US irradiation, allowing the monitoring of the formation and subsequent resealing of pores in the membrane. While the results also indicated that Ca^{2+} was necessary for resealing, the recovery time was on the order of 4 – 10 sec, which is more consistent with pore formation. They also noted a delay of the onset of transmembrane current (i.e. sonoporation) after the obliteration of added Optison®, indicating that the UCA destruction did not immediately or directly cause the sonoporation effects.[31] Similarly, Bao et al. demonstrated the benefit of using the contrast agent Albunex® to enhance transfection, but showed that the UCA was rapidly destroyed by exposure, implying that most of the effects were caused by ultrasound induced cavitation, rather than any direct influence of the Albunex®.[24] Deng et al. explain that the fragmentation or destruction of the UCA can generate secondary bubbles that act as cavitation nuclei and there is a resulting ongoing and cyclic process of bubble activity during US exposure.[31]

The potential for MEMS-based sonoporation devices was demonstrated by Siu et al., where a miniature PZT element was used to sonoporate cells in a culture plate. While the device was proof-of-concept, the possibility for remotely activated, implantable US actuators as a method for cancer therapy was introduced.[32] Marentis et al. presented a microfluidic device with a deposited ZnO minisonicator for cell lysis, but the concept could be used for microsonoporation devices as well.[33]

1.5 Combining Electroporation and Sonoporation

Based on the extensive success in both the fields of electroporation and sonoporation, investigation of the combined effect of these methods is a natural progression, however, very little has been reported to this aim. Yamashita et al. presented *in vivo* transfection into the quadriceps of mice via a plasmid DNA injection followed by electro-sonoporation. The skeletal muscle was exposed to 5 – 10 min of sonoporation and electoporated in the middle of the US exposure with a pair of electrode plates. Different electrode voltages and types of plasmid DNA solutions (0.85% NaCl vs. albumin microbubbles) were examined. With 0.85% NaCl solution, electro-sonoporation (at 25 V) increased luciferase activity in the muscle twofold compared to electroporation alone (at 25 V). When albumin microbubble solution was used, electro-sonoporation (at 10 V) increased luciferase activity in the muscle 16-fold compared to sonoporation alone. However, it is important to note that the albumin microbubbles significantly disturbed the efficacy of gene transfer through electroporation and therefore, the peak luciferase activity was observed at 25 V electro-sonoporation with 0.85% NaCl plasmid DNA solution. It is also mentioned that DNA concentration and injection volume, electroporation pulse duration and number of

pulses, and US output intensity, frequency, length, and duty cycle were all fixed. Optimization of these parameters could further improve efficacy, perhaps significantly.[34] Escoffre et al. presented a successive electro-sonoporation method *in vitro*, first electroporating CHO cells using a conventional-type setup with plasmid DNA encoding enhanced green fluorescent protein (EGFP) and then sonoporating the cells in the presence of a BR14 microbubbles. When using microbubbles, electro-sonoporated cells showed up to a three-fold increase in transfection efficiency compared to those cells that were electroporated only. When cells were electro-sonoporated without BR14, the increase in efficiency was two-fold; however, the cell viability in this case was 2.5 times greater than that of cells treated in the presence of microbubbles. Furthermore, it was observed in some cases that electroporation caused DNA aggregates to form in the cell membrane and the subsequent sonoporation step was required to induce direct propulsion into the cytoplasm. Again the need for optimization was addressed to further improve transfection efficiency.[35]

The motivation for this study is the development of a microfluidic device that simultaneously applies the conditions required for microelectroporation and sonoporation in a flow-through fashion that allows for high throughput, high efficiency transfection of mammalian cells.

2. DEVELOPMENT OF FABRICATION METHODS

2.1 Laser Micromachining

During development of a microelectroporation device, low-cost and high-resolution polymer microfabrication techniques were investigated. Polymer microdevices can be fabricated using methods such as photolithography of photosensitive polymers, hot embossing, injection molding, reactive ion etching (RIE), or replica molding by using polymers that can be cross-linked thermally or chemically.[36] The selection of processing methods is strongly dependent on the choice of materials needed for the microdevice.

Unlike other microfabrication methods, laser micromachining is versatile where almost all polymer materials can be directly ablated without the requirement of a cleanroom facility and processing equipment.[36-37] Specifically, the use of an infrared CO_2 laser allows rapid patterning of a polymer substrate at low cost. However, the minimum feature size commonly achievable using CO_2 lasers pales in comparison to those attainable with the significantly more expensive excimer lasers. Minimum reported feature sizes using a CO_2 laser commonly range from 50 – 350 μm, with an average width of 150 – 200 μm, compared to the sub-micron features feasible with excimer lasers.[37-44] CO_2 laser micromachining research has typically focused on the use of poly(methyl methacrylate) (PMMA) substrates.[38-43, 45-47] The benefits of using PMMA with CO_2 laser machining include a high infrared absorbance, a lack of soot production, and the ease of comparison to other fabrication methods like hot embossing and injection molding.[37] Some example applications of devices machined by CO_2 laser ablation include: capillary electrophoresis and blood separation chips[39], multi-layer

microfluidic structures that incorporate optical fiber technology[40], continuous flow PCR microfluidic chips[47], and microchannels for manufacturing optical bubble switches.[48]

2.2 Laser Stenciling

In order to significantly reduce the minimum feature size obtainable using a low-cost CO_2 laser micromachining tool, we have developed a laser stenciling method where a laser beam (typical spot size = 100 μm) is raster scanned across a silicon stencil having openings smaller than the laser spot to selectively pattern an underlying sample (Fig. 2.1). This results in ablated patterns on the polymer substrate with sizes corresponding to the sizes of the openings in the silicon stencil, overcoming the resolution limitation of a conventional CO_2 laser micromachining tool. More specifically, we were able to attain feature sizes on the order of 10 μm in some materials. Using a single stencil, this process can produce numerous polymer substrates with ablated micropatterns corresponding to the stencil openings; thus, we can achieve small volume production at a low cost. Similar stencils have been commonly used as masks for selective metal or dielectric deposition, ion implantation and dry etching.[49-52] Like our laser stenciling method, these configurations have been shown to effectively allow direct pattern transfer to a sample by means of a microfabricated stencil. With this laser micromachining method, we fabricated arrays of microchannels and through-holes in Kapton® and poly(dimethylsiloxane) (PDMS) films and characterized how different thicknesses and materials, as well as laser machining parameters, influence the ablated microstructures. These patterned layers were incorporated into multi-layer microfluidic devices, where individual layers were bonded together using thermal or oxygen plasma bonding.

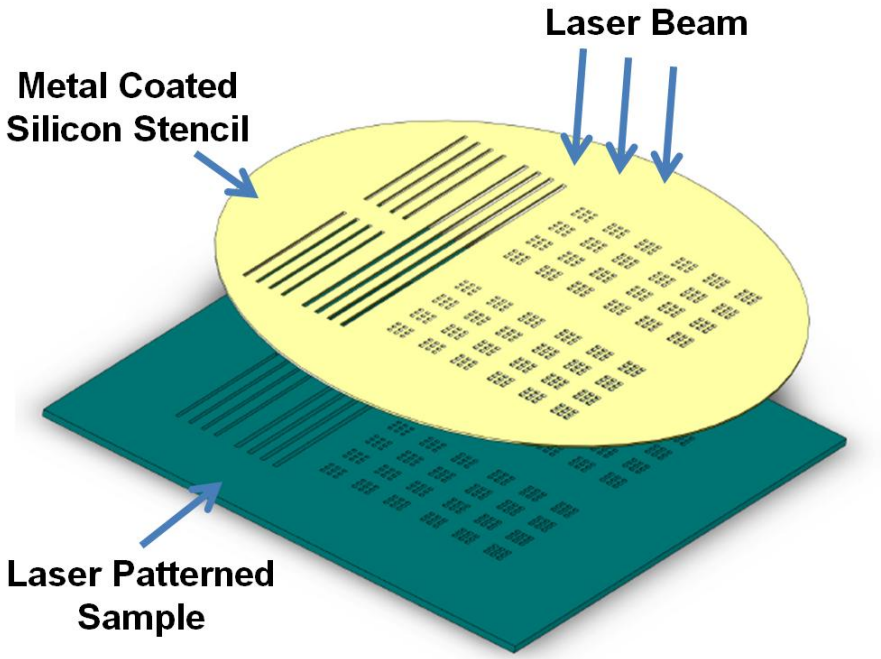

Fig. 2.1 Schematic of the laser stenciling method.

2.3 Materials and Methods

2.3.1 Stencil Fabrication

The stencils were constructed from silicon wafers (7.62 mm diameter, 380 μm thick) with LPCVD-deposited Si_3N_4 on both sides (*t* = 150 nm, Silicon Quest International, Inc., Santa Clara, CA, USA). The wafers were cleaned with Piranha solution (H_2SO_4:H_2O_2 = 3:1 (v/v)) for 15 minutes and then thoroughly rinsed with deionized (DI) water and dried with nitrogen gas. Photoresist (Microposit® S1818, Rohm-Haas-Shipley Company, Inc., Marlborough, MA, USA) was spin-coated onto the wafer at 4000 rpm for 30 sec. After a 10 min soft bake at 100°C, the wafers were loaded into a mask aligner (Karl Suss MA6 Mask Aligner, SUSS Microtec, Inc., Waterbury Center, VT, USA) and selectively exposed to UV light for a dose of 84 mJ/cm^2. The photoresist was then developed (Microposit® MF-319, Rohm-Haas-

Shipley Company, Inc., Marlborough, MA, USA) for 1 – 2 minutes, the wafers then thoroughly rinsed with DI water and dried with nitrogen, and finally hard-baked for 10 min at 135°C.

Reactive ion etching (RIE) was used to remove the exposed Si_3N_4 on the frontside of the wafer. The RIE chamber (CS-1701 Reactive Ion Etching System, March Plasma Systems, Concord, CA) was supplied with CF_4 gas at a rate of 50 sccm. The wafers were loaded into the chamber and the patterned photoresist served as an etch mask. The selected protocol removed the Si_3N_4 at a rate of 15 nm/min, thus a 10 min etch was sufficient. Post-RIE the remaining photoresist was removed with acetone.

To etch through the bulk of the silicon wafer, a 40% by weight potassium hydroxide (KOH) bath was prepared (KOH, reagent grade ≥90% flakes, Sigma-Aldrich, St. Louis, MO, USA). The KOH solution was heated and stabilized to 80°C in a hot water bath. The wafers were approximately 380 μm thick and the prepared solution etched (100) silicon at a rate of 1 μm/min. Therefore, the wafers were loaded into the KOH bath and left to etch for approximately 6.3 hours. RIE was used again to remove the entirety of the backside Si_3N_4, which was the final step in creating through-etched holes and channels in the silicon wafer. The same Si_3N_4 etching protocol was used as described above.

The final step in fabricating the stencil was metal deposition on the frontside of the wafer. Silicon is transparent to the infrared wavelength of the CO_2 laser ($\lambda \approx 10.6$ μm), thus to block the transmission of the laser through the un-etched areas of the stencil, a thin metal coating is required. The stencil wafers were again Piranha-cleaned and loaded into an electron beam evaporator. Au/Cr was deposited onto the frontside

of the stencil wafers to a thickness of 200 nm. The stencil fabrication process is illustrated in Fig. 2.2.

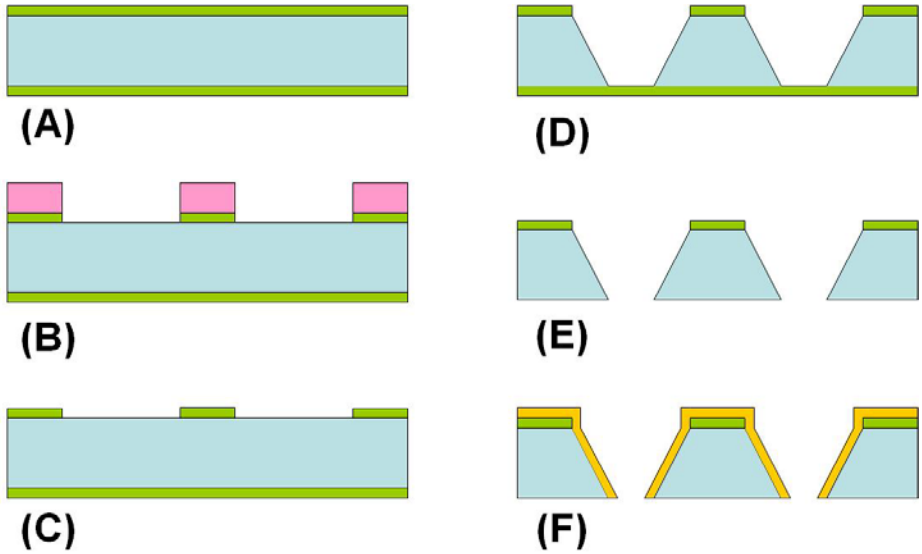

Fig. 2.2 Fabrication steps for the Si stencil. (A) LPCVD Si_3N_4 deposited Si wafer (B) Photoresist patterning and Si_3N_4 removal using RIE (C) Si wafer with topside Si_3N_4 etch mask (D) KOH etching through the Si wafer (E) removal of backside Si_3N_4 layer (F) Au/Cr coating on topside of the Si stencil.

A silicon stencil etched with KOH and tetramethylammonium hydroxide (TMAH) to form vertical sidewalls was also fabricated. To accomplish vertical sidewalls, a (110) silicon wafer was used in place of a (100) wafer. It has been demonstrated that both KOH and TMAH can etch high-aspect ratio, vertical features in (110) oriented silicon wafers, due to the vertical orientation of the (111) etch stop.[53-54] The silicon wafers (Silicon Quest International, Inc., Santa Clara, CA, USA) were deposited with PECVD silicon nitride (t = 600 nm) on both sides. A thicker film was necessary as PECVD-deposited nitride was much more susceptible to the wet etch solutions, though the TMAH etch rate of Si_3N_4 was considerably lower than that of KOH.[55] Therefore, a combination of TMAH and KOH etches was used to minimize destruction to the etch

mask while achieving high aspect ratio, vertically etched features. The photoresist patterning and Si_3N_4 removal techniques were identical to those used in the previous stencil fabrications, with the exception of a large, square-shaped well that was patterned on the backside of the wafer to help accelerate the etching process and reduce the depth of etch needed from the frontside. Thus, when submersed in the etch bath, both sides of the wafer etched simultaneously. The wafers were etched in a 5% TMAH solution (TMAH, 25 wt % in H_2O, Sigma-Aldrich, St. Louis, MO, USA) bath at 90º C for 5 hrs (etch rate: 0.5 μm/min) and then in a 40% by weight KOH bath at 80º C for 30 min (etch rate: 1.5 μm/min) to achieve fully etched through, vertical sidewall channels of varying widths. An e-beam deposition of Au/Cr was the final fabrication step, though in this stencil, the metal layer was deposited on the backside of the wafer to a thickness of 200 nm. The stencil fabrication process is illustrated in Fig. 2.3.

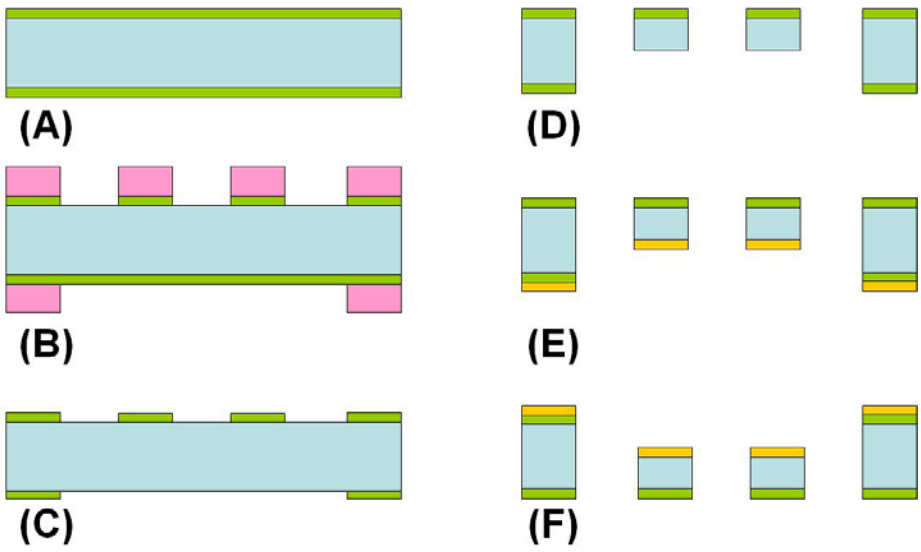

Fig. 2.3 Fabrication steps for the vertical sidewall Si stencil. (A) PECVD Si_3N_4 deposited Si wafer (B) Photoresist patterning and Si_3N_4 removal using RIE (C) Si wafer with Si_3N_4 etch mask on both sides (D) TMAH and KOH etching through the Si wafer (E) Au/Cr coating on backside of (F) flip stencil over for polymer patterning.

2.3.2 Laser Stenciling Set-up and Systems

The laser stenciling set-up is shown in Fig. 2.1. Briefly, the microfabricated stencil is placed on top of the polymer sample to be patterned. The laser beam is then raster scanned across a selected area of the stencil and the underlying sample is patterned to match the exposed stencil geometries.

The laser system used in these experiments was a computer-controlled Professional Laser Series (PLS) 6.120D Laser Engraving and Cutting System (Universal Laser Systems, Inc., Scottsdale, AZ, USA). The stencil and sample were placed upon the cutting table (812.8 x 457.2 mm work area). The lens used in these experiments has a focal distance of 50.8 mm with a minimum spot size of approximately 127 μm. The maximum output power of the beam is 60 Watts. In the stenciling application, the power never exceeded 10% of the maximum, or 6 W, with values of 4 – 6% (2.4 – 3.6 W) commonly used. The maximum engraving speed of the system is approximately 1800 mm/s. In our experiments, the standard speed used was 3% of the maximum, or 54 mm/s. These selected parameters achieved successful sample patterning without causing damage to the stencil and allowed design completion in an acceptable period of time.

The focus, power, and speed settings were controlled with the included print-driver software. A brief overview of the raster beam setup is as follows: First, drawing software was used to create a solid 2D box of a desired size, to fully cover the area to be patterned (Solidworks DWG Editor, Dassault Systèmes SolidWorks Corp., Concord, MA, USA). In the laser software, any solid objects are automatically patterned with the raster engraving mode. Next, the design was printed to the laser driver software. With this interface, the design could be moved to any location on the cutting table and

various settings (% power, % speed, PPI, focusing) could be set and adjusted. Finally, by running the program, the pattern can be transferred to the sample.

2.3.3 Polymer Substrates

The polymer substrates used in these experiments were Kapton® and PDMS films. Various Kapton® sheets were tested, including 100-E, 200-E, 200-HN, and 300-FN (DuPont Electronic and Communication Technologies, Honey Brook, PA, USA). Both Kapton® E and HN products are general purpose films, while FN products are HN films that are coated on one or both sides with a thermally-activated adhesive, Teflon® FEP fluoropolymer. Typical measured thicknesses of these samples ranged from 40 – 90 µm. PDMS (Sylgard® 184 Silicone Elastomer Kit, Dow Corning Corp., Midland, MI, USA) membranes were created by spin coating a 10:1 PDMS mixture (polymer resin : curing agent) onto a PMMA plate at speeds of 1000 – 1500 rpm for 30 – 45 sec. The resulting films were approximately 50 – 100 µm thick. In most experiments, the Kapton® and PDMS films used were on the order of 50 µm and 100 µm thick.

2.3.4 Multilayer Microfluidic Devices

To demonstrate the functionality of this new fabrication method, we present a multilayer microfluidic device with a laser stenciled channel. The top layer is the sample loading layer and serves as the ceiling for the microfluidic channel; the inlet and outlet are created in this layer by using the vector cutting mode of the laser. The middle layer is the microfluidic channel layer; the through-cut channel is fabricated in this layer with the stenciling method and is typically 1 – 2 cm in length. The bottom layer is the base and serves as the floor for the channel. We demonstrate this device using PDMS films.

The PDMS device was fabricated using an O_2 plasma bonding process. PDMS membranes were prepared and then laser patterned as described above. The films were placed on a glass slide backing layer and loaded into the O_2 plasma chamber (Expanded Plasma Cleaner, Harrick Plasma, Ithaca, NY, USA). After approximately 1 min exposure to the plasma, the samples were removed and bonded together. To bond all 3 layers, this process was done 2 times per device. The final product was placed on a glass 25 mm x 25 mm glass cover-slip for structural support and handling.

2.4 Results and Discussion

2.4.1 Silicon Stencil

The stencil was designed to have a wide range in the dimensions of the backside openings, from 10 – 100 μm. To achieve these dimensions on the backside of the wafer, frontside opening sizes were calculated with simple trigonometry based on the expected 54.7° etch angle characteristic of KOH etching. The possibility of over-etching was compensated for by including several patterns with incrementally adjusted widths for the same desired backside opening. The difference in size of immediately neighboring patterns was generally between 2 – 8 μm.

After KOH through-etching, patterns with widths greater than 20 μm were generally consistent in size and shape, while patterns smaller than 20 μm tended to be much less uniform. Therefore, we selected patterns of approximately 25 and 55 μm for the majority of the experiments that utilized the KOH-etched stencil. SEM images of a 3 x 3 array of 50 μm holes from the backside of a stencil are shown in Fig. 2.4.

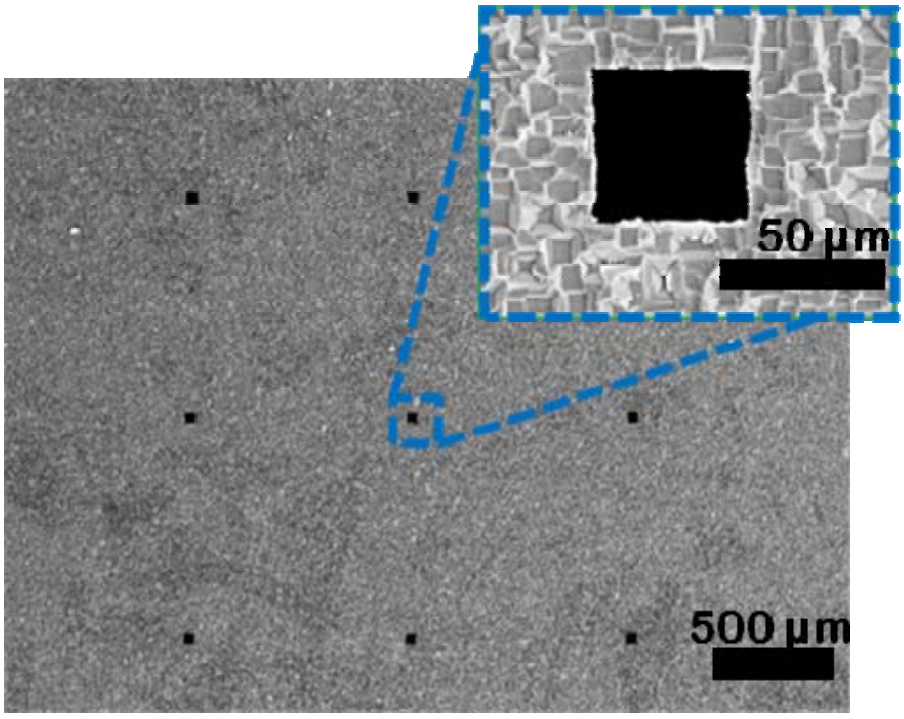

Fig. 2.4 SEM images showing the Si stencil from the backside. A 3 x 3 array of square holes can be seen. Inset shows a close-up view of a single 50 x 50 µm opening.

2.4.2 Polymer Sample Patterning

Silicon stencils with 3 x 3 arrays of square microholes and microchannels up to 2 cm in length were used. Fig. 2.5 shows some examples of resulting through-holes using a stencil pattern of 25 x 25 µm in both Kapton® and PDMS films. To achieve through-holes in the Kapton® and PDMS sheets while keeping power low enough to maintain a minimum feature size, multiple raster scanning passes were required. This method of multiple passes was used in lieu of increasing the power of the laser to minimize feature sizes and reduce stencil damage. Increasing the power of the beam had the effect of increasing the dimensions of the pattern features. This is believed to be caused by an increase in sample and stencil heating generated at higher laser

power. Additionally, at some threshold (around 15 – 20% maximum power at 3% speed), the stencil itself tends to be irreversibly damaged. The degree of this damage ranges from purely cosmetic to altering the stencil opening's size and shape to fracturing the stencil, depending on the output power selected. By instead keeping the power relatively low (1 – 10% maximum power) and running multiple passes over the area to be patterned, we could increase depth penetration in increments until a through-hole was achieved in the sample and minimized, if not eliminated, damage to the stencil itself.

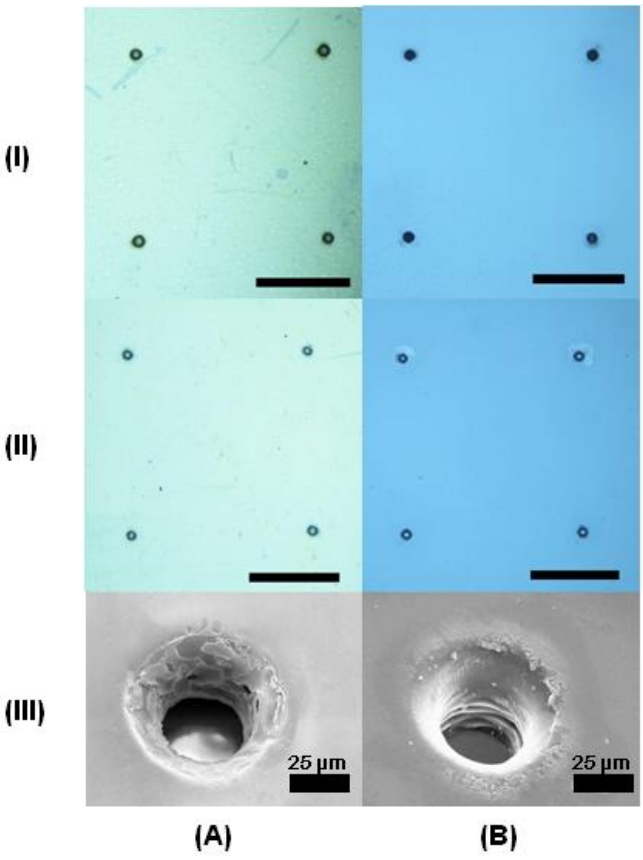

Fig. 2.5 Laser stencil machined holes. Using Si stencils with 25 µm openings in (A) 50 µm thick Kapton® films and (B) 50 µm thick PDMS films: (I) Frontside view of hole array, (II) Backside view of hole array [scale bars = 500 µm], (III) SEM of individual hole from frontside.

Fig. 2.6 shows the relationship between the number of raster scanning passes performed and the front and backside opening widths of the resulting pattern, when using 25 [(a), (b)] and 55 μm [(c), (d)] wide stencil openings. Overall, the resulting frontside opening was typically 157% of the size of the stencil opening and the backside opening was 79%, indicating that the resulting openings were shaped like a truncated cone. This is consistent with the Gaussian (or Gaussian-like) profiles commonly reported with CO_2 laser cutting[37-38, 40-43, 45, 48, 56] and results from the Gaussian intensity profile of the beam. For simplicity, we will continue to refer to these hole arrays results as conical, though they may be better approximated by a 3D Gaussian plot. Standard deviation was within 10% in most cases, showing that this method can reproducibly generate features with variations of only a few microns.

Pattern geometry of the stencil was limited due to the KOH method of etching, which produces rectangular features. However, it is important to note that while using rectangular stencil patterns, the resulting copies in the underlying sample generally consisted of rounded edges and corners. For example, square holes are translated into circular or sometime elliptical features and rectangular channels are converted to channels with rounded ends. It is also crucial to mention that there is a discrepancy between the stencil opening size and the resulting pattern size in the polymer film. One possible explanation for this outcome is the slight separation between the stencil and sample. While there is direct macroscopic contact between the two, complete and uniform contact at the microscale is not probable without a more sophisticated set-up. For example, the PDMS membranes are spun onto PMMA plates and then laser patterned. The stencil is placed directly on the PDMS membrane, but the contact of the film and the wafer is determined by the shape and topography of the PMMA plate. If

the plate does not lie perfectly flat, the stencil wafer may not lie flat on its surface. Therefore, this separation, however minor, has the potential to reduce the pattern resolution.

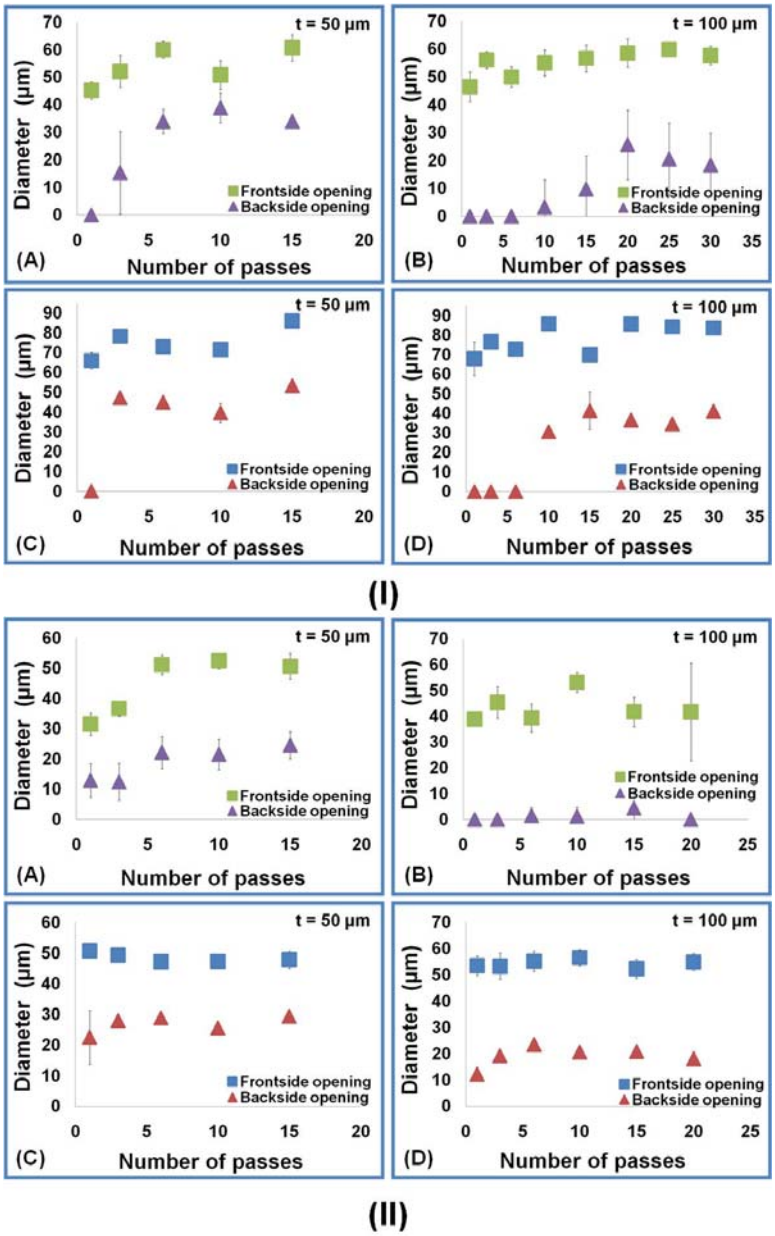

Fig. 2.6 Number of raster scanning passes vs. patterned width. Frontside and backside widths at different Kapton® (I) and PDMS (II) film thicknesses, using Si stencil having 25 µm openings [(A), (B)] and 55 µm openings [(C), (D)]. *n* = 9 for all samples.

The frontside openings of holes in Kapton® films were on average 179% the size of the stencil openings, while the backside hole openings were 95%. More specifically, 25 μm patterns had an average frontside opening of 54.4 ± 4.2 μm, or 218% the stencil opening and 55 μm patterns had an average frontside opening of approximately 76.6 ± 3.2 μm, or 139% the stencil opening. For both 50 and 100 μm thick films, frontside dimensions were approximately the same. Backside openings, however, could not be generalized for varying film thickness due to the conical profile of the through-hole. Backside openings for 25 μm patterns were on average 35.6 ± 4.2 μm (142%) in 50 μm films and 21.6 ± 12.3 μm (86%) in 100 μm films. Openings for 55 μm patterns were on average 46.2 ± 3.2 μm (84%) in 50 μm films and 36.8 ± 4.2 μm (67%) in 100 μm films. It should be noted that 25 μm patterns tend to produce features near in value or larger than the stencil opening size, while 55 μm patterns produce features near in value or smaller than the stencil opening.

Clearly, it takes fewer passes to achieve through holes in thinner films. For example, for 25 μm openings, it typically takes 6 passes to achieve through-holes in a 50 μm Kapton® film, while it takes 20 passes to achieve a through-hole in a 100 μm film. The dimension differences in the resulting backside openings of these through-holes in 50 and 100 μm thick films can be explained by the conical shape of the laser pattern. Consider an inverted, truncated cone superimposed on the cross section of a 100 μm thick film, which has a midpoint line at the 50 μm depth. The wider base of the cone represents the frontside opening, which is constant regardless of film thickness. Now, notice the width of the cone at the 50 μm (midpoint) line compared to the width at the 100 μm edge. This image represents the results we have observed. We can then hypothesize that with continued raster passes, the hypothetical cone is maintaining its

general shape and the angle of its sidewalls and is simply extended in height, thus reducing the cross-sectional area at its smaller base.

The frontside openings of holes in PDMS films were on average 135% the size of the stencil openings, while the backside hole openings were 58%. More specifically, 25 μm patterns had an average frontside opening of 44.0 ± 5.1 μm, or 176% the stencil opening and 55 μm patterns had an average frontside opening of approximately 51.4 ± 3.0 μm, or 93% the stencil opening. These approximate frontside dimensions were seen in both 50 and 100 μm thick films. Backside openings for 25 μm patterns were on average 22.7 ± 5.0 μm (91%) in 50 μm films. Though the data is not presented in the provided PDMS graphs, up to 30 raster passes were conducted upon the 25 μm pattern and still through-holes in 100 μm film were not achieved. One way to view this result is assuming that the cone reached its maximum height (until no longer truncated) and this height was shorter than the thickness of the film. Openings for 55 μm patterns were on average 26.9 ± 3.0 μm (49%) in 50 μm films and 19.0 ± 2.1 μm (35%) in 100 μm films. It should be noted that 25 μm patterns tend to produce features that are nearly true to size, but only in 50 μm films, while 55 μm patterns produce features that are less than half the stencil opening size.

Differences in resulting pattern sizes, shape, and consistency of results were compared between Kapton® and PDMS. For a particular stencil opening size, patterns in PDMS were generally smaller than those in Kapton®. Frontside openings in PDMS are truer to the stencil opening size (though still nearly double in the 25 μm case) and backside openings are typically less than or equal to the size of the stencil pattern. However, it is important to mention that patterns in Kapton® are generally much more circular than those in PDMS. The shapes of the translated patterns in Kapton® are

almost always circular, while in PDMS they tend to be more elliptical or sometimes diamond shaped. When measurements were taken, the patterns were approximated to a circular shape, resulting in added inaccuracy of the opening sizes presented above. In terms of consistency, or standard deviation, a direct comparison of the materials produces inconclusive results. In the case of the 55 μm pattern, the consistency of Kapton® and PDMS results for both frontside and backside openings were comparable (Frontside: $4.18\%_{\_KAPTON}$ vs. $5.76\%_{\_PDMS}$; Backside: $8.89\%_{\_KAPTON}$ vs. $10.95\%_{\_PDMS}$), however in the case of the 25 μm pattern, neither PDMS nor Kapton® has highly consistent results (Frontside: $7.78\%_{\_KAPTON}$ vs. $11.70\%_{\_PDMS}$; Backside: $28.76\%_{\_KAPTON}$ vs. $21.79\%_{\_PDMS}$).

A few notes should be made on overall production speed of the laser stenciling method. As mentioned previously, the raster scanning speed used was approximately 54 mm/s. Depending on the selected area to be patterned, the average processing time per sample typically ranged between 0.5 – 1.5 min. Such samples included single channels, between 1 – 2 cm in length and 3 x 3 arrays of holes, with holes spaced approximately 1 mm apart. For prototyping purposes, the stenciling method is an attractive option due to this relatively rapid production speed, though the time taken to fabricate the stencil must be taken into account as well.

2.4.3 Vertical Sidewall Stencil Comparison

In order to assess the effect of the sloped sidewalls of the KOH-etched wafer on the resulting pattern profile, we employed a wafer with vertically etched features for comparison. The stenciling method was nearly identical to that used with the KOH-etched stencil, with the small exception of flipping the stencil over to allow better contact

between the stencil and the polymer sample. Because of the large well etched in the backside, a sizable gap would be present between the stencil and the sample to be patterned if the laser was incident on the frontside.

The sloped sidewall and the vertical sidewall stencils were used to pattern channels of variable widths, in the range of 10 – 100 μm, in 100 μm thick Kapton® films. To expedite the comparison of the different stencils, the number of passes required for through-channels was minimized by increasing the laser power used. While this does not produce the optimal channel widths, it is suitable for stencil-to-stencil comparisons. The channels patterned in the polymer film showed similar sloped profiles from both stencils once a through-channel was achieved. However, the KOH-etched sloped sidewall stencil required approximately twice as much laser exposure to achieve this through pattern. For example, 1 pass at 10% power was sufficient for the vertically etched stencil, while 2 passes at 10% power were required for the sloped sidewall stencil. Furthermore, the sloped sidewall stencil became fouled with organic residue in fewer laser exposures than the vertically etched stencil, thus more cleaning steps are required to keep the stencil in working condition. For these reasons, the vertically etched stencil may be considered favorable; however, the resulting channel profile is still comparably sloped, which is likely the result of Gaussian profile of laser beam.

Fig. 2.7 shows a graphical comparison of the different stencils, assessing the width of the stencil opening versus the width of the patterned channel. From the graph, it is clear that both stencils had similar increases in the width of the patterned channel in the polymer film as the width of stencil openings increased, though the slope (i.e. discrepancy between polymer channel width and stencil channel width) was greater in the case of the sloped sidewall stencil. This indicates that these patterns are less true-

to-size than the patterns made by the vertical sidewall stencil. The dotted line represents a one-to-one relationship between stencil and pattern openings and from this reference it is evident that the vertical sidewall stencil creates backside openings that more closely match the stencil openings than the sloped sidewall stencil. Also, notable from this graph is the fact that both stencils do not pattern through channels for stencil openings smaller than 50 μm at the given conditions.

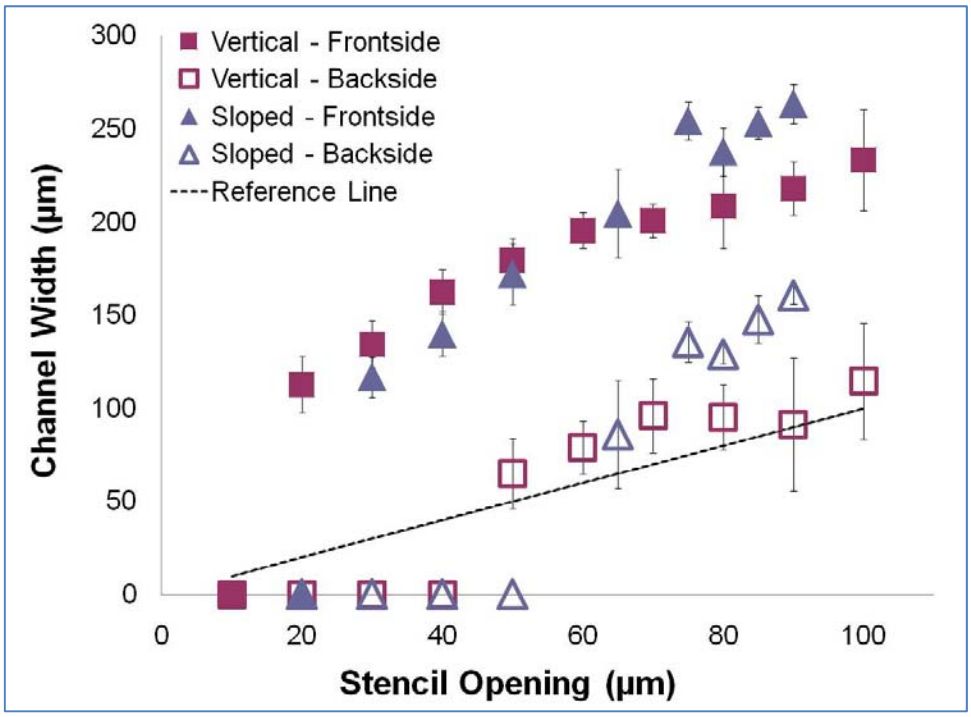

Fig. 2.7 Stencil comparison. Width of the stencil opening versus the width of the patterned channel (frontside and backside) for both vertical sidewall stencil (□) and sloped sidewall stencil (Δ) in 100 μm thick Kapton®. *n* = 4 for all samples.

It is not fully understood why stencils with more vertical sidewalls generate patterns that more closely match the size of the opening. Some possible attributors to this phenomenon may be: (1) the increase in total laser power required to achieve a through-channel in the sloped sidewall stencil (though the necessity for this increase is

not well understood) or (2) an insufficient metal coating on the sloped sidewalls of the KOH etched openings, either due to poor coverage during deposition or perhaps localized removal of the metal due to repeated laser exposure and post-exposure cleanings. Because the sloped sidewalls are exposed to the laser beam and silicon is transparent to the beam, any defects in the metal coverage in this area could result in an unintentional broadening of the perceived stencil opening size. Vertical sidewalls ensure that the only areas patterned in the sample are those directly exposed to the laser beam.

2.4.4 PDMS Multilayer Microfluidic Device

Multi-layer microfluidic devices were fabricated to illustrate a practical application of the laser stenciling method. Fig. 2.8 presents an example of the PDMS multi-layer microfluidic device. Fig. 2.8(A) presents the device components and their assembly and Fig. 2.8(B) shows a 4-channel device, where all channels were patterned simultaneously. A stencil location with four, neighboring microchannels was selected and the surrounding area was exposed to the laser by raster scanning. The total processing time required to pattern all four channels was approximately 4 min. To test the fluidic integrity of the multi-layer devices, droplets of colored dye were placed at the channel inlet and a vacuum was applied to the channel outlet. The dye occupied the channel as a result of this negative pressure. Fig. 2.8(C) is a magnified image of one of the microchannels filled with blue colored dye. In these devices, the dye solution was confined to the channel area and no leakage was observed. These results demonstrate the capability to rapidly prototype microfluidic devices with laser stenciled channels.

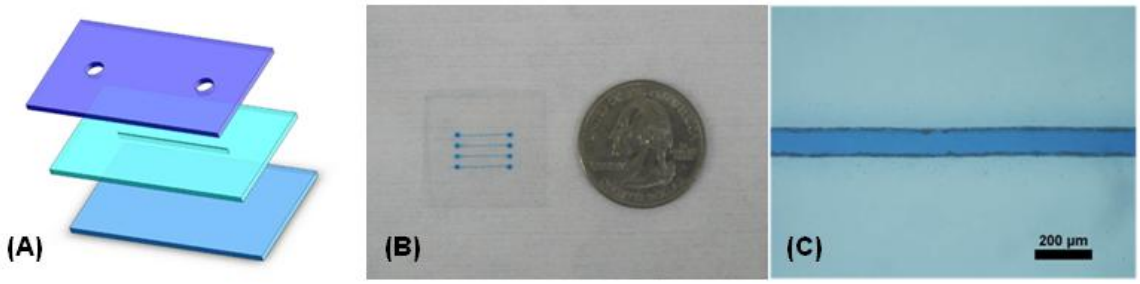

Fig. 2.8 Multilayer microfluidic devices. (A) Schematic of the three device layers [inlet/outlet, microfluidic channel, substrate layers] and assembly, (B) PDMS 4-channel device filled with blue color dye for visualization, (C) Enlarged view of the dye-filled PDMS channel (10X magnification).

3. DEVELOPMENT OF A COMBINED ELECTROPORATION AND SONO-PORATION SYSTEM

3.1 Design of Setup for Improved Cell Transfection

Given the similar nature of electroporation and sonoporation, it is reasonable to consider combining the two processes for enhanced cell membrane permeabilization. The motivation for this study was to devise a system that applies both methods simultaneously for improved overall transfection efficiency, while minimizing the cell destruction characteristic of over-exposure to either poration modality. For the electroporation element, we have designed and tested a flow-through microchip electroporator that utilizes microfabricated electrodes and microfluidic channels to determine the electric field strength and pulse duration. It was powered by a simple function generator. For the sonoporation element, an immersion-style piezoelectric transducer, driven by a function generator connected to RF power amplifier, was employed. The ultrasound transducer was placed directly on top of the electroporation microchip so that ultrasound pressure and electrical voltage pulses could be applied simultaneously to cells flowing through the microfluidic channels. This configuration also allowed cells to be monitored optically both during the procedure and afterwards through microscopy.

3.1.1 Comparison of Electrode Configurations

Different microchip electrode configurations were investigated for successful electroporation. Fig. 3.1 shows a schematic diagram of the cell flow (indicated by the arrows) relative to the electrodes for each configuration. In the first, planar electrode

configuration (Fig. 3.1 left), interdigitated electrodes were patterned onto a glass slide and cells were flown in a channel directly above them. The limitation of using planar electrodes for electroporation is clearly illustrated here. In order to generate the electric field strength required to electroporate cells while keeping the supply voltage low enough to avoid excessive bubble generation, the electrode spacing must be on the order of tens of microns apart. As illustrated, the result of this design was an electric field that was concentrated only within a few microns above the bottom of the flow channel. In other words, the field strength needed for permeabilization could be generated, but did not reach the majority of the cells flowing through the channels, resulting in very low transfection efficiency.

In the second, top-bottom electrode design (Fig. 3.1 middle), electrodes were placed above and below the cell flow channel, so that the entire channel cross section at a given point would be exposed to a uniform electric field. However, the top-bottom design had several challenges in microfabrication. The Ti/Au electrodes were patterned on PMMA substrates that sandwiched the microfluidic through-channel made in PDMS. Chemically assisted bonding was utilized to bond the electrode containing PMMA layers with the PDMS layer, however resulted in poor or inconsistent bonding and lead to many device failures during experiments. Another limitation of the top-bottom electrode configuration was the inability to monitor cells during electroporation and sonoporation due to the non-transparent electrode used. A potential solution could have been the use of transparent metal electrodes such as indium tin oxide (ITO). The third limitation was, since a piezoelectric transducer for sonoporation was to be placed on top of the microchip where the generated ultrasound wave had to be coupled into the device, there were concerns that the electrode layer could have an adverse effect on the

ultrasound wave coupling. The rigid PMMA substrate was another concern, since acoustic coupling may be more difficult compared to soft polymers such as PDMS.

The third and final design (Fig. 3.1 right), the 3D electrode configuration, overcomes these limitations. Here electroplated 3D electrodes serve both as the electric field generators in the horizontal direction, perpendicular to the cell flow, and as the sidewalls of the microfluidic cell flow channel. This design enables uniform electric field application to cells flowing through the channel, direct coupling of ultrasound waves through a single polymer substrate layer, no obstruction of microscopy viewing for cell monitoring, and robust microfabrication procedures minimizing the risk of device failure.

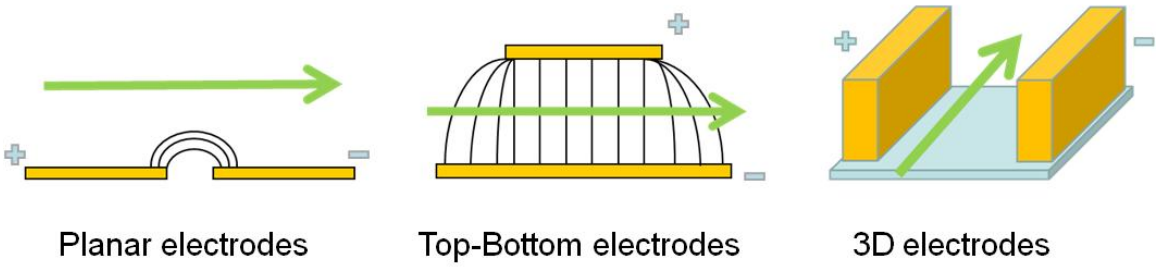

Fig. 3.1 Various electrode configurations for microelectroporation. Cell flow relative to the electrodes for each configuration is illustrated. The electrode placements are shown and the arrow indicates both direction of cell flow and approximate position in channel.

3.1.2 3D Electrode Device Design

In designing a three-dimensional electrode device, ease of fabrication was a top priority. With late stage device failures being a significant hurdle to actually performing cell experiments in the previous planar or top-bottom electrode designs, device yield was a major factor in selecting the various microfabrication techniques used here.

Layer-to-layer bonding failure resulting in leakage was a common cause for device failure during the cell experiments. Therefore, the layer-to-layer assembly of the proposed 3D electrode design relied primarily on the strong bonding between PDMS-to-PDMS or PDMS-to-glass. Oxygen (O_2) plasma treatment of these materials has been well-established as a strong, permanent bonding method. To employ this method, 3D electrodes were electroplated onto a glass substrate and a PDMS chamber was designed to fully encompass the electrodes. Fig. 3.2 shows an illustration of the design layers and their assembly. A similarly structured semi-continuous flow chip was presented by Wang et al., composed of a serpentine channel fabricated in aluminum that also served as the electroporation electrodes, which was hot embossed into a PMMA backing layer and lamination sealed to form the channel ceiling.[18]

In our preliminary experiments, cells flowing from the inlet were not fully guided into the electrode-formed channel with a straight opening, and significant amount of cells were observed to flow through the gap channels outside of the electrodes. Therefore, the inlet part of the electrode-formed channel was modified from a straight opening into a funnel-shaped opening to help capture the majority of cells flowing into the device. Furthermore, a laminar-flow based flow-focusing scheme was used to further guide all the cells into the electrode-formed channel for electroporation. Flow-focusing was achieved by a 3-way inlet, where the center channel carried cells and the two outer channels carried buffer solution to focus the cell flow into the funnel-shaped inlet.

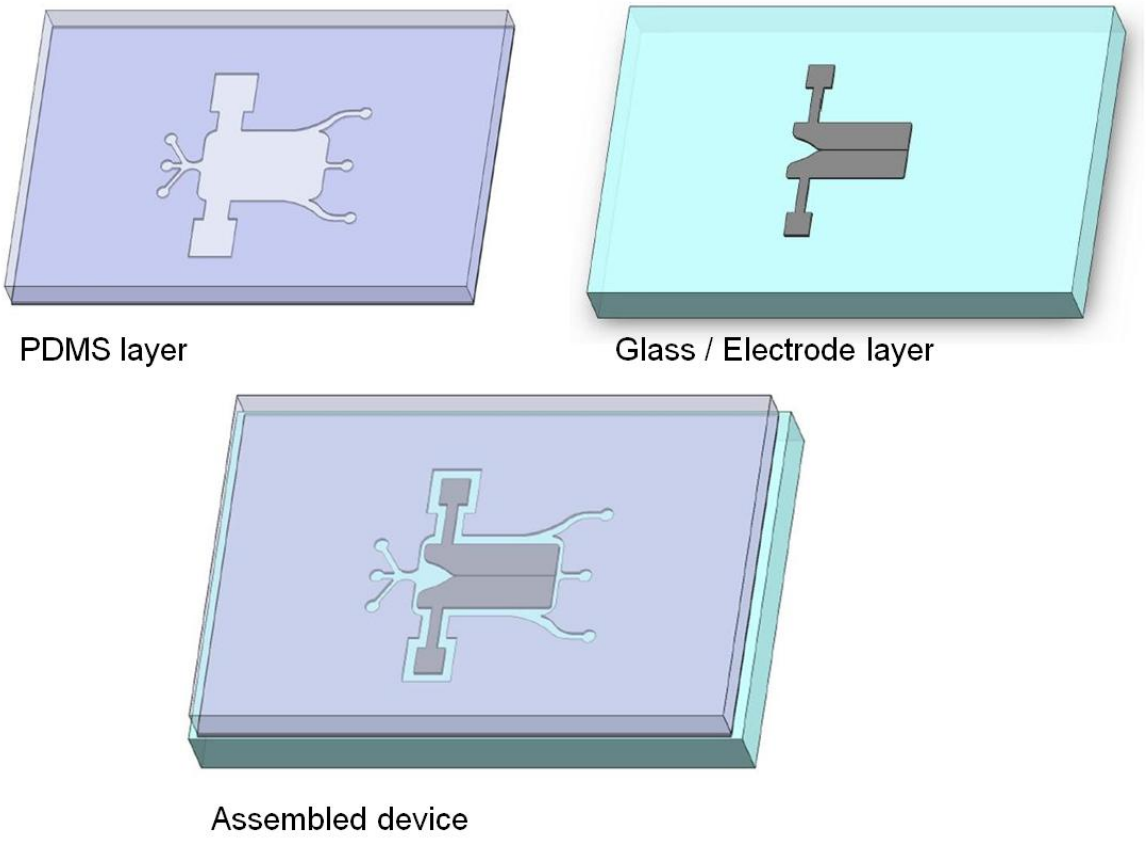

Fig. 3.2 Layers of 3D electrode device. PDMS layer contains chamber to serve as channel ceiling and outer boundaries of cell flow; optical transparency allows viewing of cell flow on chip. Glass serves as optically transparent substrate and channel floor, while plated electrodes act as channel sidewalls and electroporation actuators.

3.2 Materials and Methods

3.2.1 Fabrication of Microelectroporation Device

The planar electrodes were patterned on a glass slide using metal deposition and photolithography. Glass slides (5.08 x 7.62 cm) were cleaned with Piranha solution (H_2SO_4:H_2O_2 = 3:1 (v/v)) for 15 minutes and then thoroughly rinsed with deionized (DI) water and dried with nitrogen gas. The slides were loaded into an electron beam evaporator and Ti/Au was deposited (t_{Ti} = 200 Å, t_{AU} = 2000 Å). After an additional cleaning step, photoresist (Microposit® S1818, Rohm-Haas-Shipley Company, Inc.,

Marlborough, MA, USA) was spin-coated onto the slides at 4000 rpm for 30 sec. After a 10 min soft bake at 100°C, the glass slides were loaded into a mask aligner (Karl Suss MA6 Mask Aligner, SUSS Microtec, Inc., Waterbury Center, VT, USA) and selectively exposed to UV light for a dose of 84 mJ/cm^2. The photoresist was then developed (Microposit® MF-319, Rohm-Haas-Shipley Company, Inc., Marlborough, MA, USA) for 1 – 2 minutes, the slides were then thoroughly rinsed with DI water and dried with nitrogen, and finally hard-baked for 10 min at 135°C. Poly (dimethylsiloxane) (PDMS) channels were fabricated using soft lithography. The master mold was made of patterned SU-8 photoresist (SU-8 2025, MicroChem Corp., Newton, MA, USA) on silicon wafers (Silicon Quest International, Inc., Santa Clara, CA, USA). The wafers were cleaned with Piranha solution, rinsed with DI water, and dried with nitrogen gas. The SU-8 resist was spin-coated onto the wafers at 2400 rpm for 30 sec. After a soft bake of 10 min at 65°C and 20 min at 95°C, the wafers were loaded into a mask aligner (Karl Suss MA6 Mask Aligner, SUSS Microtec, Inc., Waterbury Center, VT, USA) and selectively exposed to UV light for a dose of 174 mJ/cm^2. The photoresist was baked post-exposure at the same conditions as the soft bake and then developed (Microposit® Thinner P, Rohm-Haas-Shipley Company, Inc., Marlborough, MA, USA) for 4 – 5 minutes. The slides were then thoroughly rinsed with IPA and dried with nitrogen. A 10:1 PDMS (Sylgard® 184 Silicone Elastomer Kit, Dow Corning Corp., Midland, MI, USA) mixture (polymer resin : curing agent) was degassed and poured onto the mold, and after baking at 85°C for 30 min, an inverted copy of the mold was formed. The PDMS layer was bonded to the glass/electrode slide using an O_2 plasma bonding process. Both the PDMS and glass samples were loaded into the O_2 plasma chamber (Expanded Plasma Cleaner, Harrick Plasma, Ithaca, NY, USA) and after approximately

1 min exposure to the plasma, the samples were removed and bonded together. Electrical connections were supplied via wires soldered to the contact pads built into the electrode design.

The top-bottom electrodes were fabricated using the same process as described above for the planar electrodes, but the substrate used was PMMA instead of glass. The channel layer was a PDMS membrane, but the channel itself was laser-machined, not molded. Bonding the PMMA and PDMS layers required a chemical gluing method, which involved soaking the one layer in 3-Aminopropyltriethoxysilane (APTES) solution and one layer in 3-Glycidoxypropyltrimethoxysilane (GPTMS) solution for 20 min after O_2 plasma treatment. This method previously reported by Lee and Chung has been shown to give good bonding between PDMS-PDMS and PDMS-poly(ethylene terephthalate) (PET).[57] The layers were then rinsed with DI water, dried with nitrogen gas, and placed in a hot press (40°C) for approximately 1 hour. An additional PDMS block layer was bonded for fluidic connections. Electrical connections were supplied via wires bonded to the PMMA layers with silver paste (Silver Paste Plus, SPI Supplies, West Chester, PA, USA) to the contact pads on the top electrode and the solid bottom layer electrode. Silver paste was used in lieu of solder because the soldering gun easily melted the PMMA layers and destroyed the electrodes.

The 3D electrodes were patterned on glass slides by electroplating. Originally, the device was designed for copper (Cu) plated electrodes, but further experiments showed a dark residue forming between the electrodes when an electric field was applied, which in turn inhibited cell flow through the electrode channel and completely obstructed any viewing of the device performance with a microscope. Therefore, the plated material was switched to nickel (Ni) and no residue issues were observed.

Glass slides were cleaned and loaded into the electron beam evaporator as described above and a Au/Cr seed layer was deposited (t_{AU} = 2000 Å, t_{CR} = 200 Å). After an additional cleaning step, photoresist (Futurrex NR2-20000P, Futurrex, Inc., Franklin, NJ, USA) was spin-coated onto the slides at 500 rpm for 10 sec and 2700 rpm for 30 sec. After a 15 min soft bake at 150°C, the glass slides were loaded into a mask aligner (Karl Suss MJB3 Mask Aligner, SUSS Microtec, Inc., Waterbury Center, VT, USA) and selectively exposed to UV light for a dose of 1800 mJ/cm^2. The photoresist was baked post-exposure for 10 min at 80°C, developed (Futurrex RD6, Futurrex, Inc., Franklin, NJ, USA) for 5 – 10 minutes, and then thoroughly rinsed with DI water and dried with nitrogen. The resist patterned slides were then electroplated using a commercially available nickel electroplating solution (Techni Nickel Sulfamate RTU, Technic Inc., Cranston, RI, USA) for 2 hours at a current density of 20 mA/cm^2 for a resulting Ni thickness of 30 μm. The photoresist masking layer was removed with acetone and the Au/Cr seed layer was etched away with diluted Au and Cr etchants. A PDMS chamber was fabricated and served as the channel top layer. Silicon wafers were patterned with SU-8 photoresist as described above and served as master molds for the PDMS layer. Uncured PDMS was cast onto these molds, degassed, and baked as detailed previously. The inlet and outlet holes, as well as holes to expose the electrical contact pads, were formed using various sized punch tools and then the PDMS was bonded to the Ni plated area and the glass slide substrate by O_2 plasma treatment. Electrical connections were supplied via wires soldered to the contact pads built into the electrode design. Uncured PDMS was poured into the electrical contact via holes and baked at 85°C for 30 min. This PDMS not only helped secure the contact wires in place, but also provided a fluidic seal on the outside edges of the plated electrodes. This eliminated

waste flow in this area to ensure the majority of the cells passed between the plated electrodes. The 3D electrode device fabrication process is illustrated in Fig. 3.3.

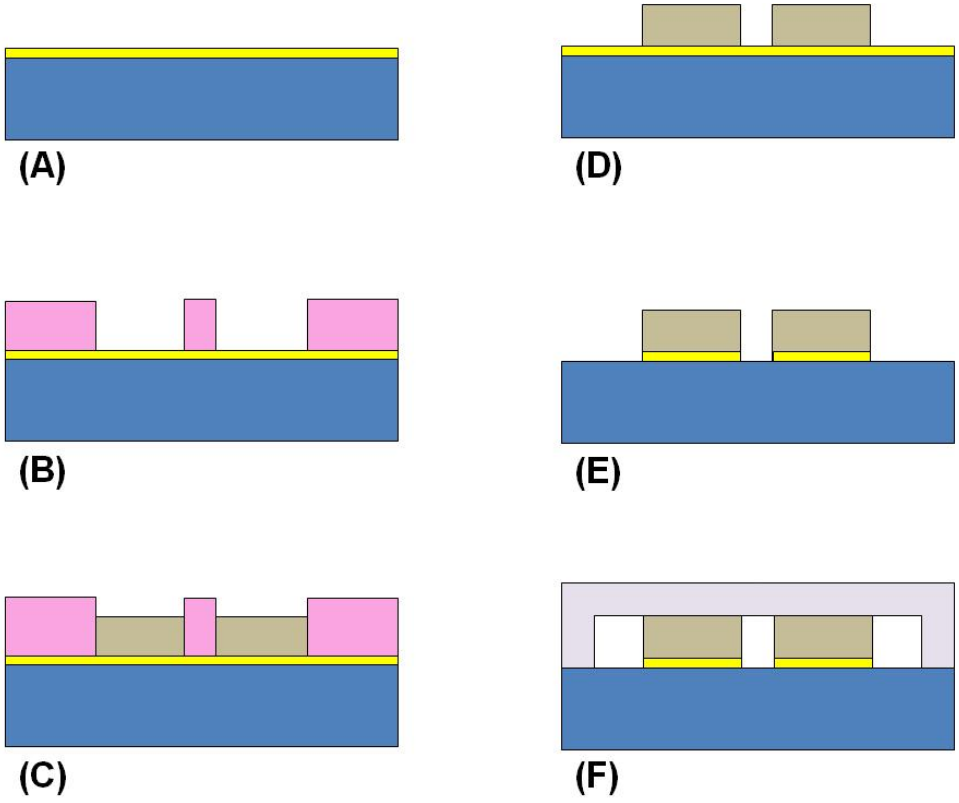

Fig. 3.3 Fabrication steps of 3D electrode device. (A) Au/Cr film layer deposited on glass slide (B) Photoresist patterning to serve as plating guide (C) Electroplating Ni (D) Removal of photoresist (E) Wet etch removal of Au and Cr seed layers (F) O_2 plasma bonding of PDMS and glass/electrode layers.

In all cases, the electroporation microchips were designed to have a PDMS layer for application of the ultrasound transducer. PDMS was selected because it more closely matches the acoustic impedance of the gel and immersion transducer than glass or rigid polymers. Fig. 3.4 shows a photograph of a completed 3D electrode device, with all electrical and fluidic connection ports added.

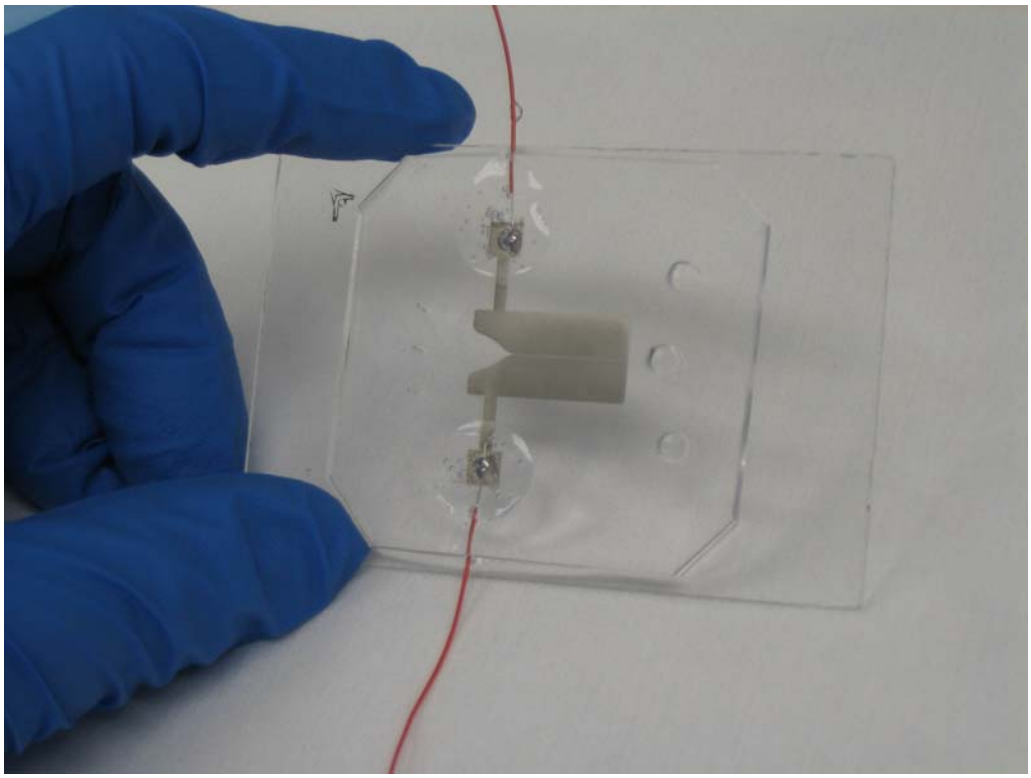

Fig. 3.4 Assembled microelectroporation device.

3.2.2 Cell Preparation

Human cervical cancer (HeLa) cells (ATCC; American Type Culture Collection, Manassas, VA, USA) were grown to 80 – 90% confluence in a 37ºC, 5% CO_2 incubator. To prepare the cells for use, first Dulbecco's Modified Eagle Medium (DMEM, Hyclone, Thermo Scientific, Logan, UT, USA) and trypsin-EDTA (Trypsin, 0.25% with EDTA 4Na, Invitrogen, Carlsbad, CA, USA) are warmed in a 37ºC water bath. Medium from the tissue culture flask (T25, 25 cm^2 cell culture flask, BD Falcon, Bedford, MA, USA) is removed with an aspirator, the flask is rinsed with sterile phosphate buffer saline (PBS) (pH 7.4, Invitrogen, Carlsbad, CA, USA), and 1 mL of the trypsin-EDTA is dispensed into the flask. Once it is visually determined with a microscope that all cells have

detached from the flask, 7 mL of fresh medium is dispensed into the flask to stop the trypsin-EDTA; the mixture is transferred to a 15 mL centrifuge tube and centrifuged at 800 rpm for 5 min. The supernatant is carefully removed with the aspirator and the cells are resuspended in 2 mL of fresh medium. A hemocytometer is used to verify the target cell density of approximately 2 – 5 x 10^6 cells/mL. Approximately 200 µL of the cell solution is transferred into a culture flask with 5 mL of new medium, for a 1:10 splitting ratio for subculture. The remaining 1 mL of cell solution is transferred to a 1.5 mL microcentrifuge tube and 50 µL of propidium iodide (PI) for a concentration of 1:20 (v_{DYE}:v_{MED}) (1 mg/mL in DI H_2O, Invitrogen, Carlsbad, CA, USA) and 1 µL of Calcein AM for a concentration of 5 µM (Calcein AM in DMSO, Invitrogen, Carlsbad, CA, USA) are added and thoroughly mixed with pipetting. Here, PI was used as the material to be delivered into the cell, where Calcein AM was used to check the viability of the cells.

3.2.3 Electroporation Methods

The electric field strength (E) in the flow channel is determined by the following equation:

$$E = \frac{V}{d}$$

where V is the applied voltage and d is the distance between electrodes which, in the proposed design, is also the width of the channel. To achieve the desired E-field range for HeLa cell electroporation (0.3 – 2.3 kV/cm), and help prevent cell clogging in the channel, the distance between the electrodes was designed to be 50 µm.[58-60]

The voltage source used was an analog function generator (GFG-8210, GW Instek America Corp, Chino, CA, USA). An alternating current (AC), square wave was

used in all experiments with a peak-to-peak amplitude of 5 V, 8 V, or 10 V and a frequency of 1 kHz or 100 kHz. The duty cycle was 50% in all experiments. The conditions above were selected based on calculation and the electrolysis threshold of phosphate buffer saline (PBS). Prior to cell experiments, we examined the performance of the electrode channel by flowing PBS solution (pH 7.4, Invitrogen, Carlsbad, CA, USA) in the device and varying the applied voltage parameters. At a frequency of 1 kHz, the threshold for bubble generation at the electrodes was approximately 5.2 Vpp; however, by increasing the frequency of the waveform to 100 kHz, bubble generation was not observed with an applied voltage as high as 10 Vpp. Ziv et al. demonstrated that bubble generation, or electrolysis, can be reduced by using an AC source (in place of DC) and is frequency dependent (shorter frequencies are preferred).[7] Fox et al. stated that electrolysis can be further reduced by applying bipolar pulses, making the time-averaged current zero. Electrolytic reactions still occur, but are partially reversed in the successive pulse.[8] Avoiding electrolysis is of utmost importance in our design, as the bubbles produced can rapidly obstruct the entire flow channel, which can cause permanent device failure. Therefore, the applied voltage was kept in the range of 8 – 10 Vpp at 100 kHz in all electroporation experiments.

The flow rate in the microfluidic device was controlled using two separate syringe pumps. The cell solution was loaded into a 1 mL syringe (BD Tuberculin Slip Tip Syringe, 1 mL, Becton, Dickinson and Company, Franklin Lakes, NJ, USA) and connected to the device with 0.30 inch OD silicone tubing (Tygon S-54-HL medical plastic tubing, Saint-Gobain PPL Corp., North Clearwater, FL, USA) inserted into the PDMS top layer through a punched inlet opening. The cell solution was driven by a single syringe pump (KDS100 Infusion Pump, KD Scientific Inc., Holliston, MA, USA) at

a flow rate of 0.01 – 0.1 ml/hr. In our initial design, this was the only means of flow control; however, we observed a substantial cell flow-widening effect in the funnel area preceding the electrode flow channel. This attributed to a high incidence of cell flow above the electrodes rather than between them. Cells flowing above the electrodes were partially caused by an imperfect height match between the electroplated electrodes and the PDMS cell flow channel.

To improve cell flow in the device, we altered our design to have cell flow focusing into the channel using sheath flow. To accomplish this, we added two inlet branches on either side of the cell flow channel to continuously inject a buffer solution with an additional syringe pump (Pump 11 PicoPlus, Harvard Apparatus, Holliston, MA, USA). For buffer solution, PBS was introduced at a typical buffer-to-cell-flow ratio of 2:1. With this modification, a notable increase in the amount of cell flow in the electrode channel was observed. To further maximize the cell flow in the channel, the height of the plated electrodes and the chamber in the PDMS layer were measured at multiple locations for each device to better match and improve the contact between the layers.

Precisely controlling the flow rate is essential as it determines the cell exposure time to the electric field. In order to maintain a constant cell stream, the minimum cell flow rate we could use was 0.01 ml/hr (with a 0.02 ml/hr sheath buffer flow). At lower flow rates, cells were not adequately propelled through the tubing and connectors. The maximum flow rate employed, with either buffer or cell solutions, was 0.5 ml/hr, as higher rates often compromised the integrity of the electrode-to-PDMS bond.

Prior to each cell experiment, the microfluidic channel was treated with a series of surface treatment steps to avoid cell adhesion to the channel surfaces. Before initial use of the device, deionized (DI) water was flown at a rate of 0.2 ml/hr for 10 min to

rinse and remove any remaining residue that may be present in the channel. The channel was then coated with a bovine serum albumin (BSA) solution to prevent cell adsorption to the Ni plated sidewalls. BSA was dissolved in PBS to a 5% concentration and flown in the channel for 10 min at a rate of 0.2 ml/hr and then left to sit for 1 hr. The BSA solution was injected for an additional 10 min and then PBS was used for a final rinsing step for 10 – 20 min at 0.2 ml/hr. For each electroporation experiment, the cell solution was initially injected at a rate of 0.1 ml/hr to verify the existence of cell flow in the device and confirm the effect of flow focusing. The flow was then adjusted to the desired rate and voltage was applied once conditions appeared stable. Cells exposed to the electric field were then collected at the outlet. The collection time required for each sample of 50 – 100 µL varied with the selected flow rate, but was typically on the order of 10 - 20 min. The collected cells were then incubated for 1 hr at 37ºC, 5% CO_2.

3.2.4 Sonoporation Methods

A 1 MHz piezoelectric immersion transducer (TSI–I–#300, Techno Scientific Inc., Concord, ON, CA) was driven by a function generator via a power amplifier. An immersion style transducer was chosen because the acoustic impedance of PDMS (1 ~ 1.9 MRayl) is close to that of water (~ 1.5 MRayl), and also close to that of biological tissue (1.3 ~ 1.7 MRayl).[61-62] In lieu of an immersion setup, we employed an impedance matching gel (Aquasonic 100 Ultrasound Transmission Gel, Parker Laboratories, Inc., Fairfield, NJ, USA) at the interface of the transducer and the PDMS layer.

The function generator (Agilent 33220A 20 MHz Function/Arbitrary Waveform Generator, Agilent Technologies, Santa Clara, CA, USA) supplied a 1 MHz sine wave and peak-to-peak amplitudes ranging from 10 – 100 mVpp. The signal from the

function generator was amplified by a 50 dB power amplifier (E&I 2100L RF Amplifier, Electronics & Innovation Ltd, Rochester, NY, USA). To avoid overheating of the transducer and to improve cell survival rates, we limited the continuous on-time of the transducer to 5 min at a driving voltage of approximately 15 Vpp.

Sonoporation experiments were conducted in the same device as the one used for microelectroporation. The same device preparation steps were taken and sonoporation experiments were performed at the same flow conditions and parameters as outlined above in the microelectroporation methods. With a cell flow rate of 0.01 ml/hr (with 0.02 ml/hr sheath buffer flow), the ultrasound transducer was applied through the impedance matching gel continuously for 5 min. The transducer area covers the entire flow channel and funnel area, resulting in an individual cell exposure time of 10 – 20 s. The treated cells were then collected at the outlet; the collection time required for each sample of 50 – 100 µL was typically on the order of 15 - 20 min, requiring 3 – 4 separate 5 min treatments, with 2 min cooling intervals between each continuous exposure. The collected cells were then incubated for 1 hr at 37ºC, 5% CO_2.

3.2.5 Combined Microelectroporation and Sonoporation

With our device design, integration of microelectroporation and sonoporation, or electro-sonoporation[34-35], is simple and allows for simultaneous cell exposure to both treatments. The same device preparation steps were taken and electro-sonoporation experiments were performed at the same flow conditions and parameters as outlined above in the microelectroporation and sonoporation methods. With a cell flow rate of 0.01 ml/hr (with a 0.02 ml/hr sheath buffer flow), the electric and ultrasonic fields were

applied simultaneously using the aforementioned methods. The treated cells were then collected at the outlet. The collection time required for each sample of 50 – 100 µL was typically on the order of 15 - 20 min, requiring 3 – 4 separate 5 min treatments, with 2 min cooling intervals between each continuous exposure. The collected cells were then incubated for 1 hr at 37ºC, 5% CO_2. A schematic of the experimental setup is shown in Fig. 3.5.

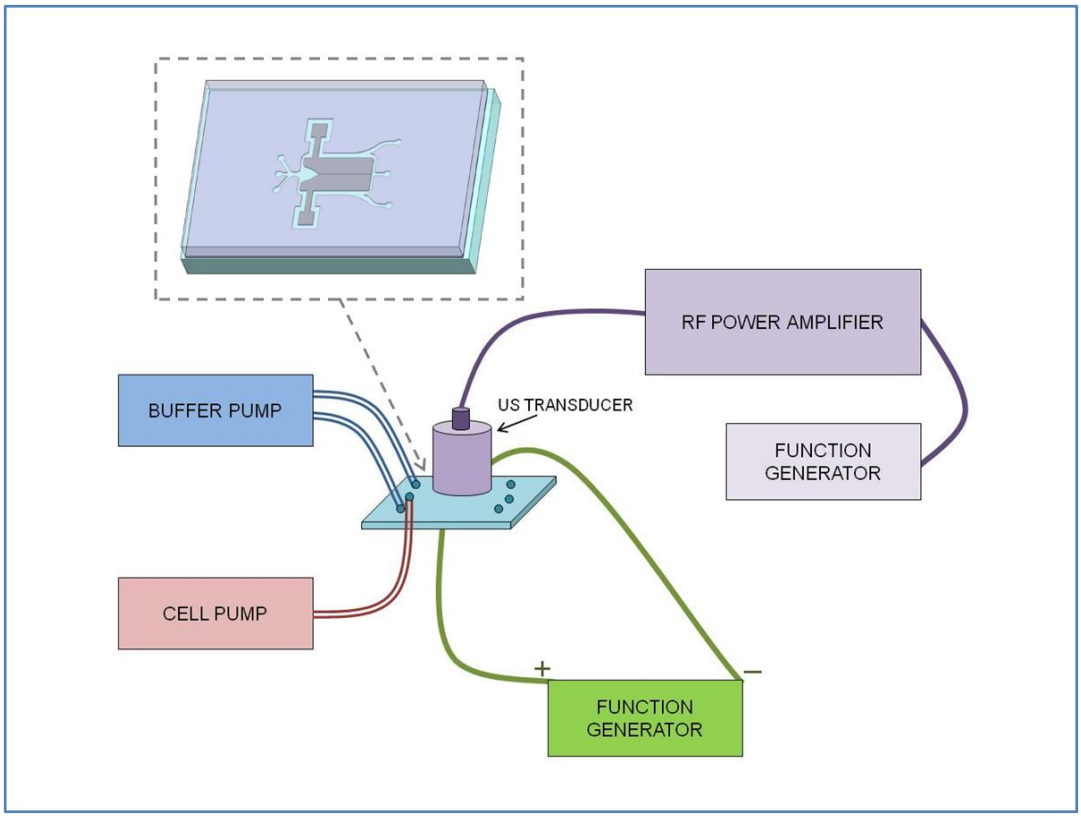

Fig. 3.5 Schematic of electro-sonoporation method. Fluidic connections are indicated by (=) and electrical connections are indicated by (–).

3.2.6 Cell Imaging and Analysis

Cells were removed from the incubator and a pipette was used to dispense droplets onto glass slides (25x75 mm Micro Slides, VWR International, Radnor, PA,

USA), which were then topped with a glass cover slip (22x22 mm Micro Cover Glass, VWR International, Radnor, PA, USA). The cells were analyzed with an inverted microscope (Nikon Eclipse TS100, Nikon Instruments Inc., Melville, NY, USA) with a green fluorescent filter (EF-4 B-2E/C FITC Filter, Chroma Technology, Inc., Bellows Falls, VT) for Calcein AM staining and a red fluorescent filter (EF-4 G-2E/C TRITC Filter, Chroma Technology, Inc., Bellows Falls, VT) for PI incorporation into cells. Bright field and fluorescent images were taken with a CCD digital camera (DS-2Mv Camera Head, NIS-Elements BR software, Nikon Instruments Inc., Melville, NY, USA) at 20X magnification.

All live cells are stained by Calcein AM (green fluorescent) and all cells with porous or compromised membranes are stained by PI (red fluorescent). Thus, cells that fluoresce both red and green are deemed to be successfully porated, or transfected, by means of electroporation or sonoporation or both. Cells that are only fluorescing green indicate that these cells are alive, but without successful poration, whereas cells that are only fluorescing red indicate that these cells were either dead from the beginning or died during the poration process. The number of transfected cells were counted and compared against the total number of cells and the total number of live cells to determine to efficiency of the poration methods.

3.3 Results and Discussion

3.3.1 3D Electrode Device Testing

Upon initial flow testing with cell solution, it became apparent that good contact between the Ni plated electrode layers and the PDMS was a necessity. Poor contact between these layers presented a few scenarios that led to device failure. The

existence of a sizable layer-to-layer gap, due to the imperfect height control between the electroplated metal and the depth of the PDMS chamber during fabrication, promoted cell flow in this path of least resistance. One scenario, shown in Fig. 3.6 (A), was the cell flow bending to pass above one electrode or the other and missing the electrode flow channel completely. This was believed to be caused by a significant gap (>15 – 20 μm) between layers coupled with a discrepancy in height or surface characteristics of the two electrodes. This can be best explained by uneven electroplating or perhaps a difference in surface roughness. Another scenario was the cell flow passing though the electrode channel area, but also above electrode areas nearest the channel. This was attributed to insufficient layer-to-layer contact in the channel area. A significant gradient in the overall height of a single electrode from outside edge to channel edge (from 50 to 25 μm) was noted. This is believed to be due to some mild delaminating of plated electrodes along the outside perimeter of the plating area. Removal of the Au and Cr seed layers was more difficult in the channel area, requiring longer etch times that tended to over-etch the electrodes' outside perimeters. Therefore, if the PDMS chamber height is matched to the maximum measured heights of the electrodes, there will exist a significant layer-to-layer gap near the channel.

Despite the different origins of these issues, both could be corrected by matching the PDMS chamber heights to be within ~ 5 μm of the minimum electroplated Ni heights, which were always located near the channel area. Devices that were fabricated with this method showed no flow bending and little-to-no above electrode flow. An example of successful focusing and elimination of cell flow above the electrodes is shown in Fig. 3.6 (B). It is important to note from 3.6 (A), that despite

successful flow focusing, the existence of a significant layer-to-layer gap will cause device failure.

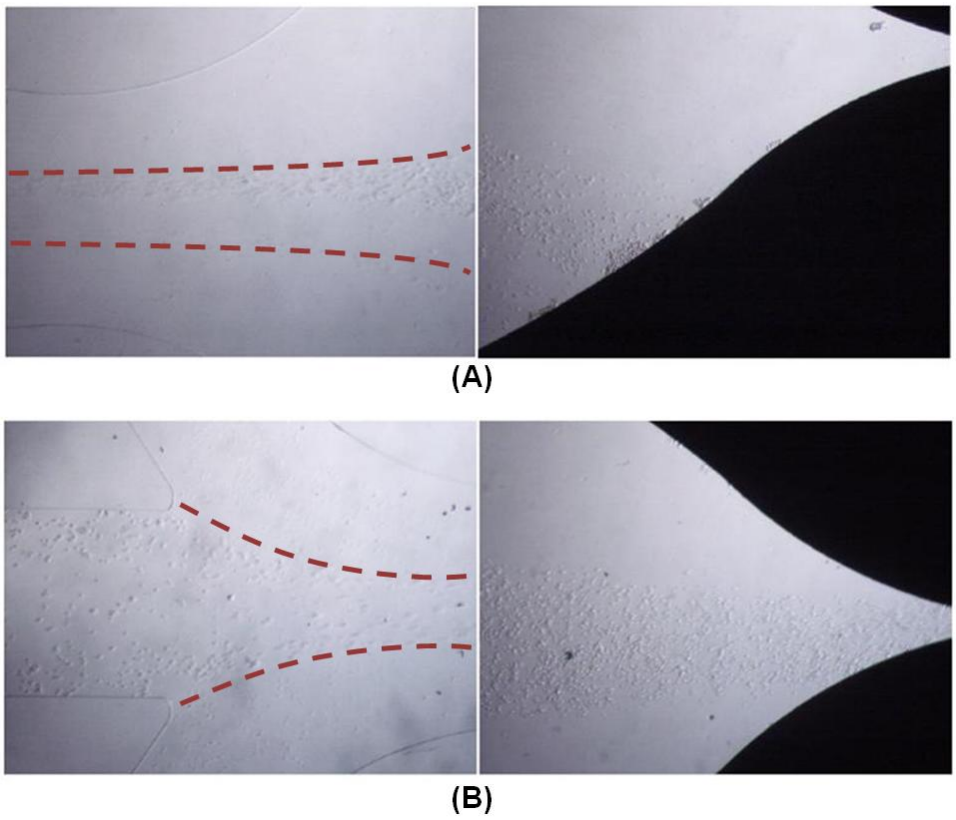

Fig. 3.6 Flow focusing results. Cell flow paths in 3D electrode device: (A) Cell flow focusing succeeded by flow bending to pass over bottom electrode (B) Cell flow focusing shown at inlet junction succeeded by concentrated cell flow in funnel area and into electrode-formed channel.

3.3.2 Microelectroporation

As the fabrication of the microelectroporation device was being optimized, there were some clear instances of over-the-electrode cell flow in initial experiments. This was the result of poor contact between the PDMS and plated Ni layers. As a consequence, untreated cells would often end up in the main channel outlet, rather than the waste outlets, and therefore influence the overall transfection efficiency for the

experiment. Fig. 3.7 shows example images from such an experiment. Fig. 3.7(A) shows both brightfield and fluorescent images of a cell sample where it is apparent, due to lack of PI fluorescence, that a sizable percentage of cells were not electroporated. The enlarged image (Fig. 3.7(B)) further illustrates the low transfection efficiency observed, which was measured to be 29.62% in this case. Cell viability was measured to be 94.90%.

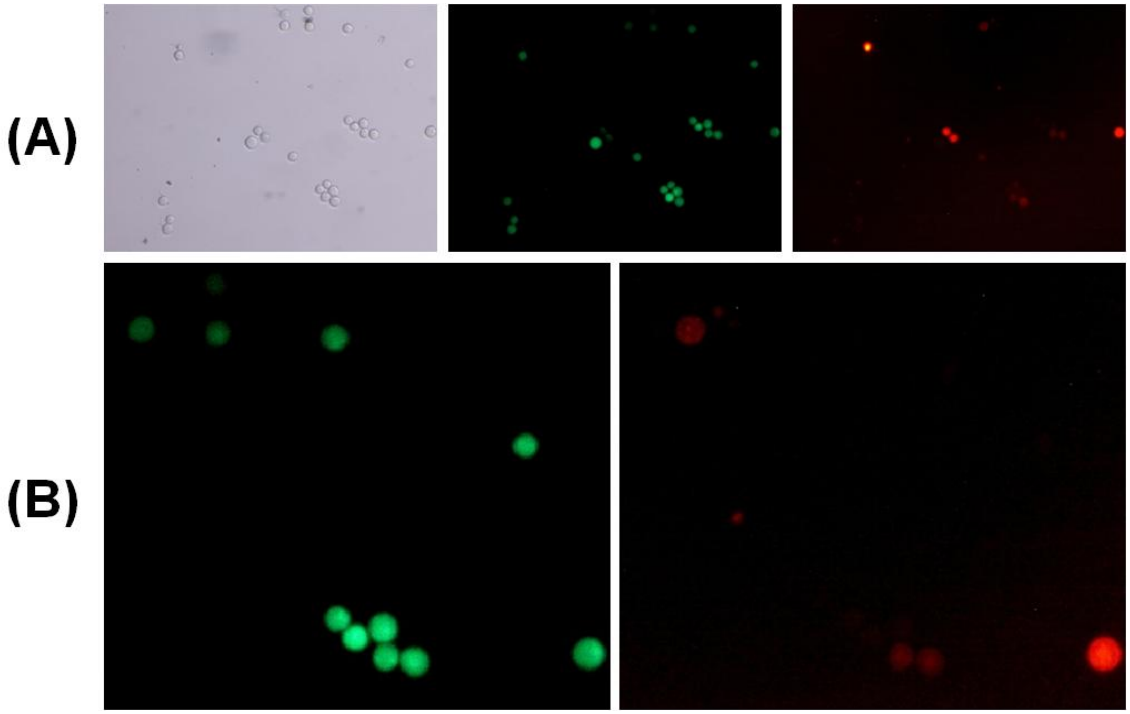

Fig. 3.7 Low efficiency microelectroporation in early device. (A) Brightfield and fluorescent images of live cells stained by Calcein AM (middle panel) and electroporated or non-viable cells stained by PI (right panel) [20X magnification]; (B) Enlarged fluorescent images for better visualization of transfection efficiency. Efficiency = 29.62%, Viability = 94.90%.

Once the device fabrication procedure was more consistent and waste flows into the main channel outlet were effectively eliminated, a vast improvement in electroporation efficiency was observed. Fig. 3.8 shows example images of a

successful microelectroporation experiment, where all collected and analyzed cells were confined to the main flow channel and exposed to the electric field. An improvement in transfection efficiency can be clearly seen in both the original micrograph images (Fig. 3.8(A)) and the enlarged images (Fig. 3.8(B)). In this particular field of view, 100% of cells were both live and successfully electroporated. The transfection efficiency was 70.87% and cell viability was 92.23%. The average efficiency through 3 different runs, on 3 different days, using 3 different devices was 70.79% ± 6.9% (n_{EXP} = 3, n_{CELLS} = 743) and the average viability of these experiments was 94.14% ± 1.7% (n_{EXP} = 3, n_{CELLS} = 743).

Optimal electroporation was observed at an applied voltage of 8 Vpp, which translates to a theoretical electric field magnitude of 800 V/cm. This value is well within the range of reported HeLa cell electroporation. Attempts to improve transfection efficiency by increasing the applied voltage to 10 Vpp (E_{THEOR} = 1 kV/cm) resulted in a significant decrease in cell viability (data not shown). Individual devices could be used for multiple experiments, as long as no irremovable clogs were formed during the course of the experiment. Due to the rough plated Ni edges and limit on maximum flow rate to maintain device integrity, this was occasionally an issue. However, in devices that were used in multiple experiments, no electrode degradation as a consequence of electrolysis was observed. Degradation was a substantial problem in earlier, gold thin-film electrode based designs, with electrodes regularly cracking and breaking apart in the channel. This issue is not evident in our current plated-electrode design.

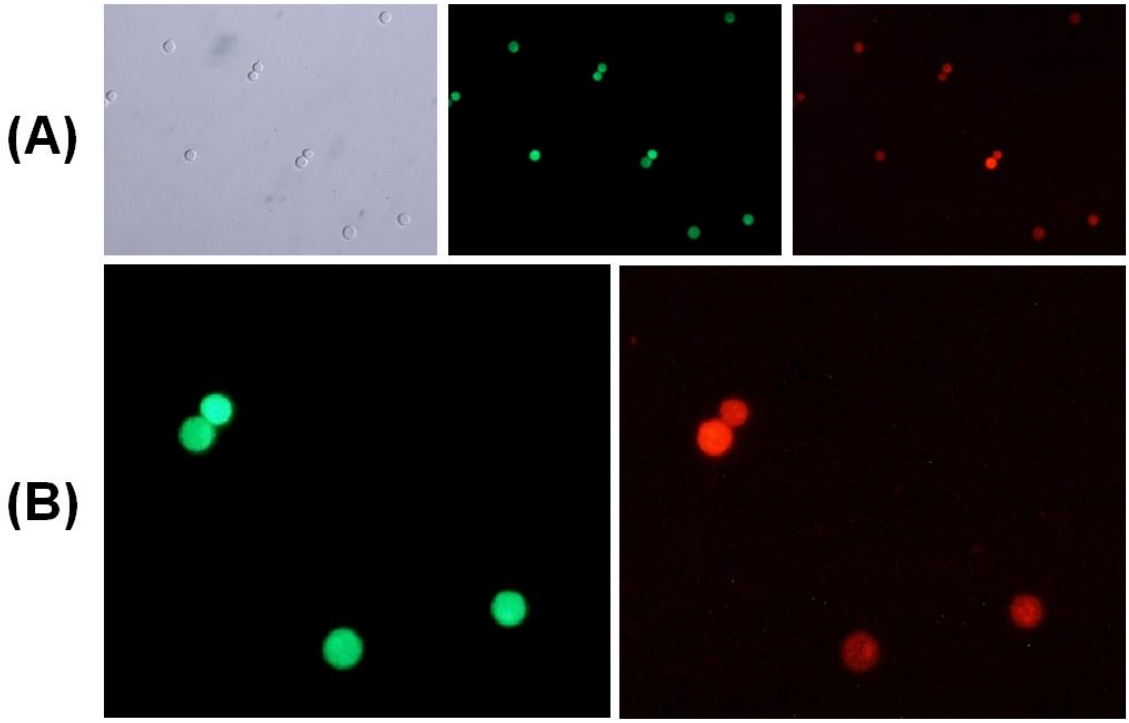

Fig. 3.8 Microelectroporation results from improved device. (A) Brightfield and fluorescent images of live cells stained by Calcein AM (middle panel) and electroporated or non-viable cells stained by PI (right panel) [20X magnification]; (B) Enlarged fluorescent images for better visualization of transfection efficiency. Efficiency = 70.87%, Viability = 92.23%.

3.3.3 Sonoporation

Sonoporation experiments were performed in the same devices used for electroporation experiments and Fig. 3.9 shows example images of a successful sonoporation experiment, where all collected and analyzed cells were exposed to an ultrasonic field by means of a manually applied US transducer. Fig. 3.9(A) and the enlarged images in Fig. 3.9(B) illustrate the resulting sonoporation rate. The transfection efficiency was 67.04% and cell viability was 96.65%. The average efficiency through 3 different runs, on 3 different days, using 3 different devices was

66.43% ± 5.3% (n_{EXP} = 3, n_{CELLS} = 353) and the average viability of these experiments was 96.99% ± 0.4% (n_{EXP} = 3, n_{CELLS} = 353).

As previously mentioned, reported sonoporation data often involves the incorporation of microbubbles or UCAs to enhance cavitation and in turn, improve transfection efficiency. However, in electro-sonoporation reports, Yamashita et al. reported an important negative side effect of using microbubbles to improve the sonoporation efficiency, where a significant increase in the resistance to electric pulses was observed, thus limiting electroporation.[34] Escoffre et al. did not report such a phenomenon in their findings, yet they did demonstrate that the improvement between electro-sonoporation and electroporation was significant with or without the use of microbubbles.[35] Therefore, the decision was made not to use microbubbles in our experiments, though it remains a possible option for future work. One important stipulation for achieving sonoporation without UCAs is the presence of a standing wave, which occurs when the US beam is reflected from an interface and merges with the progressive beam to boost the acoustic pressure in the field. This condition is easy to achieve, in fact difficult to eliminate, *in vitro*, but much more difficult to accomplish *in vivo*, so this must be considered for evolution of these methods.

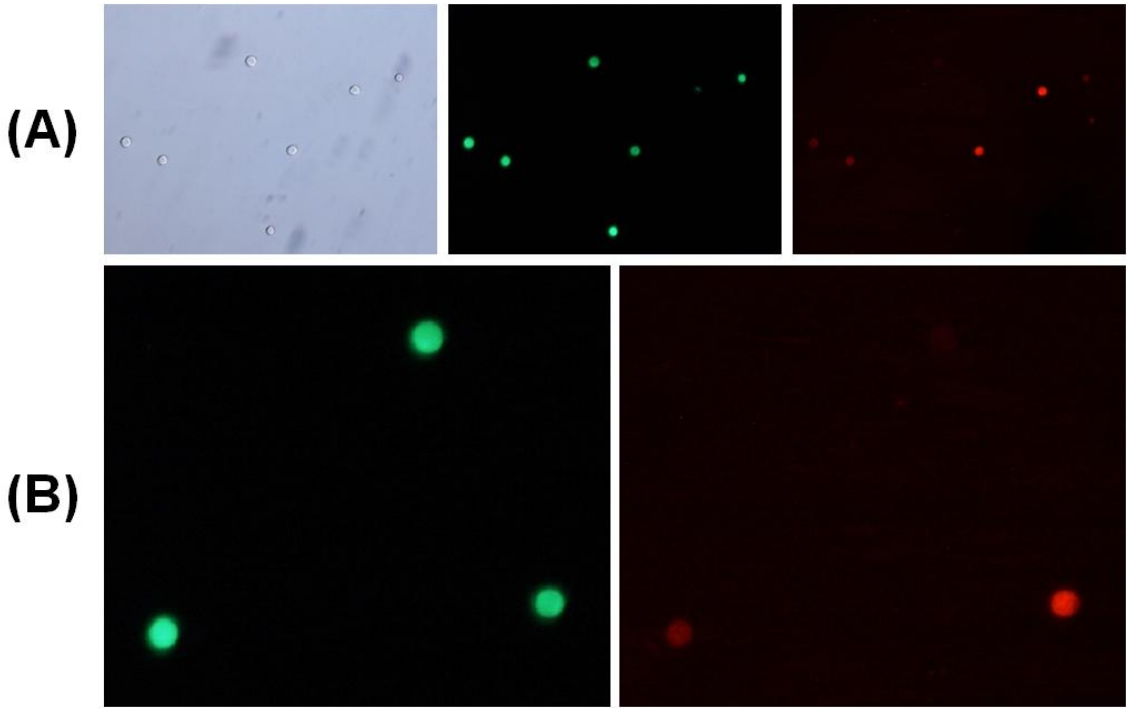

Fig. 3.9 Sonoporation results. (A) Brightfield and fluorescent images of live cells stained by Calcein AM (middle panel) and sonoporated or non-viable cells stained by PI (right panel) [20X magnification]; (B) Enlarged fluorescent images for better visualization of transfection efficiency. Efficiency = 67.04%, Viability = 96.65%.

3.3.4 Combined Microelectroporation and Sonoporation

Electro-sonoporation experiments were executed simultaneously exactly how microelectroporation and sonoporation were performed individually using the same devices. Fig. 3.10 shows example images of a successful electro-sonoporation experiment, where all collected and analyzed cells were exposed to both an electric and ultrasonic field concurrently. Fig. 3.10(A) and the enlarged images in Fig. 3.10(B) illustrate the resulting combined transfection rate. The transfection efficiency was 87.91% and the cell viability was 96.26%.

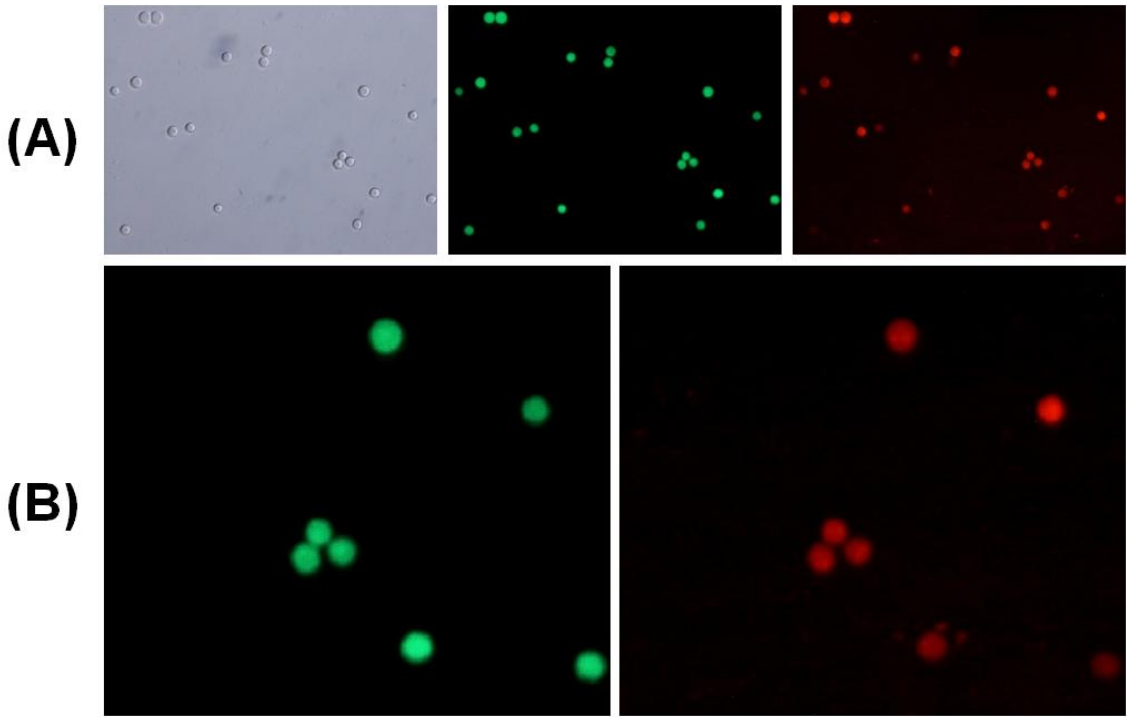

Fig. 3.10 Electro-sonoporation results. (A) Brightfield and fluorescent images of live cells stained by Calcein AM (middle panel) and electro-sonoporated or non-viable cells stained by PI (right panel) [20X magnification]; (B) Enlarged fluorescent images for better visualization of transfection efficiency. Efficiency = 87.91%, Viability = 96.26%.

The experimental results shown in Fig. 3.8, 3.9, and 3.10 are from a single batch of cells and were performed in immediate succession of one another. Therefore, analysis of these data provides an accurate comparison of the different transfection methods, without any batch-to-batch variations to be considered. Fig. 3.11 graphically illustrates this single batch comparison. The transfection efficiency of electroporation and sonoporation were quite similar (70.87% vs. 67.04%), differing by less than 4%. The efficiency for electro-sonoporation, however, was approximately 20% greater (or 31% improvement) than that of sonoporation alone (87.91% vs. 67.04%) and 17% greater (or 24% improvement) than that of electroporation alone (87.91% vs. 70.87%). Furthermore, there is very little difference in short term cell viability between the three

methods (E: 92.23%, S: 96.65%, E+S: 96.26%), showing that combining physical transfection modalities does not necessarily indicate a risk to cell health.

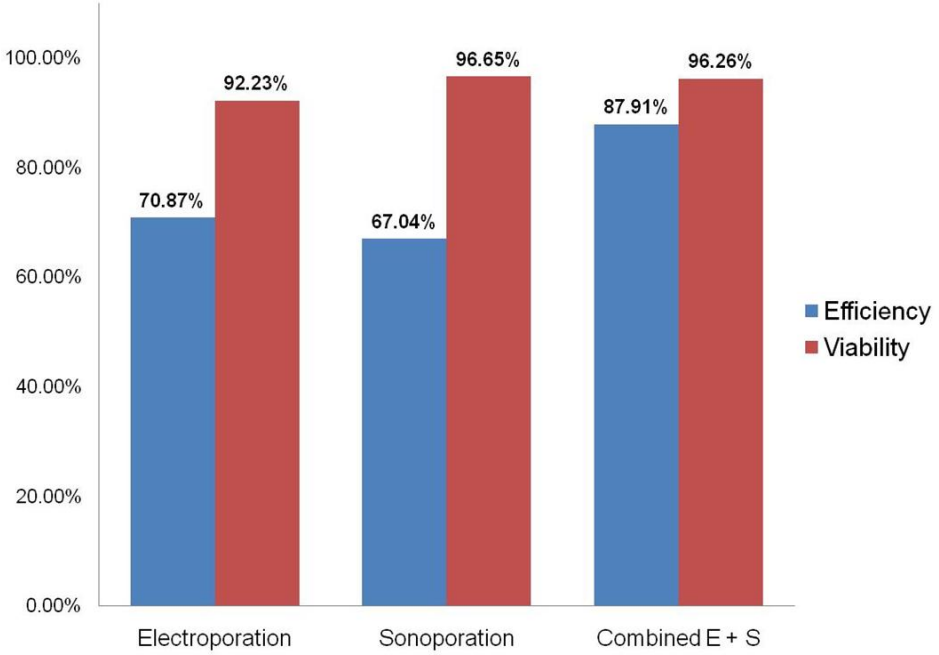

Fig. 3.11 Single batch comparison of transfection efficiency and cell viability.

The average transfection efficiency of electro-sonoporation was 81.25% ± 7.8% (n_{EXP} = 3, n_{CELLS} = 1095). The average viability of electro-sonoporation was 91.56% ± 8.9% (n_{EXP} = 3, n_{CELLS} = 1095). Figure 3.12 shows the differences in transfection efficiency and viability when using electroporation alone, sonoporation alone, and electro-sonoporation. The transfection efficiency of electroporation and sonoporation were still shown to be fairly similar to one another (70.79% ± 6.9% vs. 66.43% ± 5.3%). The overall efficiency for electro-sonoporation was approximately 15% greater (or 22% improvement) than that of sonoporation alone (81.25% ± 7.8% vs. 66.43% ± 5.3%) and 10% greater (or 15% improvement) than that of electroporation alone (81.25% ± 7.8% vs. 70.79% ± 6.9%). These improvements (Student's *t*-test, p_S = 0.031, p_E = 0.079) in

transfection are not as substantial as those seen in the single batch comparison, but here we must take into account batch-to-batch variations, such as the effects of separate cell populations and different devices (with micron-sized variations in electrode spacing/channel width).

Short-term cell viability remains high (above 90%) for all three methods as well (E: 94.14% ± 1.7%, S: 96.99% ± 0.4%, E+S: 91.56% ± 8.9%). For control, cells were pumped through the microfluidic device at the same flow rate used for all transfection methods without being exposed to any electric or ultrasonic fields, and incubated following the same protocol used for all modalities. The cell viability for this control was 98.50% by Calcein AM staining and 98.33% by PI staining (n_{CELLS} = 599).

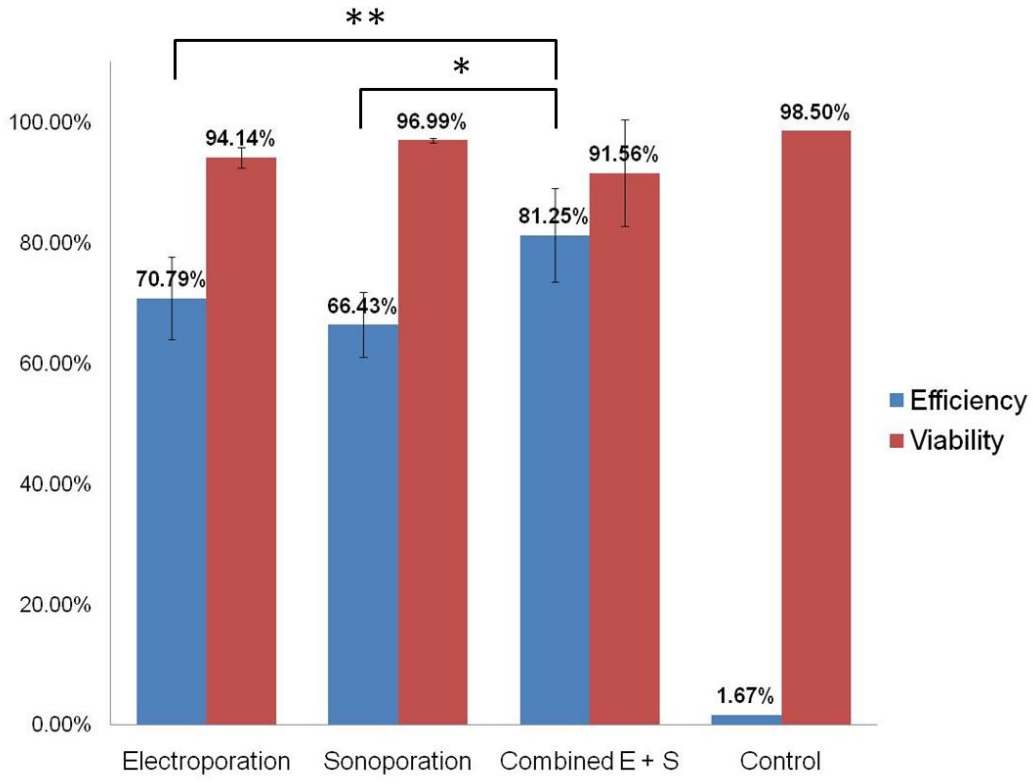

Fig. 3.12 Average transfection efficiency and cell viability for multiple experiments [n_{EXP} = 3, n_{CELLS} > 350]. Positive and negative controls shown [n_{CELLS} = 599]; *p_S=0.031, **p_E=0.079.

3.3.5 Comparison to Previously Reported Electroporation and Sonoporation Results

In order to effectively compare our electro-sonoporation device results to other configurations, the existing literature was reviewed for reported HeLa cell transfection efficiencies and viabilities. In fact, a primary reason for selecting HeLa cells for our experiments was the availability of reported electroporation and sonoporation results to compare our findings against. A summary of the transfection efficiency and cell viability data for HeLa cell electroporation is shown in Table 4.1. Conventional electroporation and microelectroporation results are isolated, and an obvious advantage of microelectroporation is evident in both transfection efficiencies and cell viabilities. The improvement in efficiency between the conventional and micro-chip methods is almost two-fold. Kim et al. provided an accurate comparison of macro- and micro-electroporation for HeLa cells exposed to similar electric field strengths.[63] At an electric field of 32.5 kV/cm, cells electroporated by the conventional setup had an approximate transfection efficiency of 40% with cell viability at 67%. Micro-electroporated cells, at an electric field of 32 kV/cm, had an approximate transfection efficiency of 85% with cell viability at 77%.[63] Again, a two-fold increase in efficiency is observed with a simultaneous improvement in cell viability. Comparing our microelectroporation results to other electroporation reports for HeLa cells, our data is in the top bracket for transfection efficiency and outperforms others in cell viability. When comparing our electro-sonoporation method to any of the various reports on electroporation, it proves to be among the highest reported in both transfection efficiency and cell viability. However, it is important to note that a direct comparison across all data in the table may not be appropriate, as different methods are used for assessing transfection efficiency.

Table 4.1 HeLa cell electroporation transfection efficiencies and cell viabilities in reviewed literature.

	Electroporation						**Electro-sonoporation**
	Conventional			**Microelectroporation**			
Researcher	*Glahder et al.* †[64]	*Kim et al.* †[63]	*Rodamporn et al.* ‡[59]	*He et al.* ‡[65]	*Kim et al.* †[63]	***This Work*** ‡	***This Work*** ‡
Transfection Efficiency	40%*	40%*	48.74%	75%*	85%*	**70.79%**	**81.25%**
Cell Viability	25%*	67%*	---	80%*	77%*	**94.14%**	**91.56%**

* Percentages not mentioned explicitly in text, values estimated from graphs

† EGFP as transfection indicator; ‡ PI as transfection indicator

Namely, a distinction must be made between using fluorescent dye and genetic expression (primarily with EGFP) as indicators of transfection. In Table 4.1, Glahder et al.[64] and Kim et al.[63] used EGFP while the reported data shown for Rodamporn et al.[59], He et al.,[65] and our work all used PI as a poration indicator. Thus, by comparing the results from the latter group, a significant improvement from macro-[59] to micro-electroporation[65] is still evident and our microelectroporation results are comparable to those reported by He et al.[65] Furthermore, comparing our electro-sonoporation results to the other reports using PI, it is evident that our method performs favorably in both transfection efficiency and cell viability.

A summary of the HeLa cell findings for sonoporation is shown in Table 4.2. Again, it should be noted that a direct comparison of all results may not be valid due to the different methods used for assessing transfection efficiency. In Table 4.2, all results shown, with the exception of our data for both sonoporation and electro-sonoporation, used some sort of genetic material for the transfection assay. However, Lai et al.[66] used DNA-FITC molecules, which merely assess uptake (similar to dyes), not genetic expression (all others[67-69] used EGFP). When comparing our sonoporation results with Lai et al.,[66] the improvements in both efficiency and viability are substantial, approximately two-fold in both cases. In fact, our results, along with those reported by Rodamporn et al.,[69] greatly outperform all others in the table in transfection efficiency. When examining the experimental protocol, it seems that the basis for this large improvement is similar to the reasons for improvements between electroporation and microelectroporation. Similar to our design, Rodamporn et al. performed sonoporation in a microfluidic chamber[69]. Microelectroporation utilizes a microfluidic platform to greatly reduce electrode-to-electrode spacing and thus generate a highly uniform

Table 4.2 HeLa cell sonoporation transfection efficiencies and cell viabilities in reviewed literature.

	Sonoporation					**Electro-sonoporation**
	Conventional			**Microsonoporation**		
Researcher	*Feril et al.* †[67]	*Chen et al.* †[68]	*Lai et al.* ‡[66]	*Rodamporn et al.* †[69]	***This Work*** ‡	***This Work*** ‡
Transfection Efficiency	16.1%	26%	35%*	68.9%	**66.43%**	**81.25%**
Cell Viability	80%*	50-60%	45%*	77%	**96.99%**	**91.56%**

* Percentages not mentioned explicitly in text, values estimated from graphs

† EGFP as transfection indicator; ‡ fluorescent dye as transfection indicator

electric field; similarly, we use a microfluidic scheme to manipulate a suspension of cells into a uniform layer, so that all cells are in relatively the same acoustic plane. The amount of exposure of a population of cells in a microfluidic channel to the applied acoustic field is highly uniform when compared to cells exposed in well-type suspensions. Thus, we term this configuration as microsonoporation. Similarly, Kinoshita et al. compared sonoporation results for suspensions of cells versus cell monolayers.[25] Using Calcein as a transfection indicator in C166 cells, at the same acoustic conditions, monolayers of cells showed an increase in efficiency of approximately 10% and a 50% improvement in cell viability compared with those treated in suspensions. Comparing our microsonoporation results to other reports for HeLa cells, it performs favorably, similar to the results from Rodamporn et al.[69] Furthermore, when comparing our electro-sonoporation method to any of the various reports on sonoporation, it excels in both transfection efficiency and cell viability.

3.3.6 Future Work

It is important to note that while we use the word ‘transfection’ as a general term for successful transient poration or wounding of the cell membrane, the word is normally reserved specifically for introducing genetic material into cells. In this study, we have not yet attempted to promote the uptake of genetic material by electro-sonoporation, but this is the natural next step. It is common for microelectroporation studies to first investigate the cellular uptake of dyes before moving on to DNA or proteins. Such studies are necessary, in the future, in order to truly determine the transfection rate achievable by our setup and method.

Furthermore, once genetic transfection is accomplished, long term cell viability studies are required. Because we used fluorescent dyes, only an investigation into short term viability was feasible. These studies will give better insight to the long-term effects of our experiments on treated cell populations and determine if there are currently unnoticed or unforeseen risks to cell health. Other improvements to the experimental protocol include device and parameter optimization. Improvements to the design of the microfluidic device and the fabrication procedure may produce more reliable, longer lasting chips that are suitable for multiple uses without the potential current issues of poor adhesion between layers, irreversible channel clogging, and dead volume near the channel opening. Another unique device alteration that should be considered is the incorporation of a MEMS piezoelectric actuator to induce sonoporation. Other groups have proven the capability of a miniaturized sonicator and this would elevate the device to a lab-on-a-chip system.[32-33] Optimization of parameters to improve transfection efficiency and cell viability should also be considered. The current parameters were selected as the best conditions of microelectroporation and

sonoporation individually. For example, the applied electroporation voltage and frequency were those that best avoided bubble generation and minimized cell death and the sonoporation driving voltage was chosen to ensure the prolonged integrity of our US transducer. However, further improvements to electro-sonoporation transfection efficiency, while maintaining high cell viability, may be achieved by making small adjustments to these parameters or others, such as cell flow rate.

4. CONCLUSIONS

In this study we have presented a proof-of-concept microfluidic device for combined microelectroporation and microsonoporation to improve overall transfection efficiency for mammalian cells. The flow-through microfluidic platform utilizes lateral 3D electrodes that function as both the electric field applying electrodes and as a cell-flowing channel structure. This novel design enables uniform electric field application to cells flowing through the metal channels as well as direct coupling of ultrasonic waves generated from a piezoelectric transducer applied at the topside through an acoustic impedance matching layer. With this device, cells flowing through the microchannel can be simultaneously exposed to an electric field and ultrasonic waves for combined microscale electro-sonoporation. Using HeLa cells, a maximum transfection efficiency of 87.91% was achieved, 20% higher than microsonoporation alone and 17% higher than microelectroporation alone. On average, the microscale electro-sonoporation showed an efficiency of 81.25%, 15% higher than microsonoporation alone and 10% higher than microelectroporation alone. In all cases, cell viability was maintained at higher than 90%. Our combined electro-sonoporation method shows similar or better transfection efficiency when compared to previously reported microelectroporation results for HeLa cells, while exhibiting more than 15% higher cell viability, and demonstrates transfection efficiency more than 12% higher than the best previously reported HeLa cell sonoporation result, while maintaining significantly higher cell viability. While others have reported electro-sonoporation protocols, to the best of our knowledge, we are the first to incorporate microelectroporation, which has been well-established to be advantageous to conventional electroporation, with sonoporation.

Overall, we have presented a proof-of-concept device to combine microelectroporation and microsonoporation in a microfluidic, flow-through format that, in its current form, meets or outperforms the transfection efficiency and cell viability standards set by other reported electroporation and sonoporation methods.

.

REFERENCES

1. M. Khine, A. Lau, C. Ionescu-Zanetti, J. Seo and L. P. Lee, *Lab on a Chip*, 2005, **5**, 38 - 43.
2. Y. Huang and B. Rubinsky, *Sensors and Actuators A*, 2003, **104**, 205 - 212.
3. Y. C. Lin, M. Li, and C. Wu, *Lab on a Chip*, 2004, **4**, 104-108.
4. Y. C. Lin, C. M. Jen, M. Y. Huang, C. Y. Wu and X. Z. Lin, *Sensors and Actuators B*, 2001, **79**, 137 - 143.
5. H. Y. Wang and C. Lu, *Analytical Chemistry*, 2006, **78**, 5158 - 5164.
6. W. G. Lee, U. Demirci and A. Khademhosseini, *Integrative Biology* 2009, **1**, 242-251.
7. R. Ziv, Y. Steinhardt, G. Pelled, D. Gazit, and B. Rubinsky, *Biomedical Microdevices*, 2009, **11**, 95-101.
8. M. B. Fox, D.C. Esveld, A. Valero, R. Luttge, H.C. Mastwijk, P.V. Bartels, A. van den Berg, and R.M. Boom, *Analytical & Bioanalytical Chemistry*, 2006, **385**, 474-485.
9. Y. Huang and B. Rubinsky, *Biomedical Microdevices*, 1999, **2**, 145 - 150.
10. Y. S. Choi, Y. J. Kim, M. Im, B. G. Kim, K. S. Yun and E. Yoon, *19th IEEE International Conference on MEMS*, Istanbul, 2006, 466 - 469.
11. S. K. Kim, J. H. Kim, K. P. Kim and T. D. Chung, *Analytical Chemistry*, 2007, **79**, 7761 - 7766.
12. K. S. Huang, Y. C. Lin, K. C. Su and H. Y. Chen, *Biomedical Microdevices*, 2007, **9**, 761 - 768.
13. H. Y. Wang and C. Lu, *Biotechnology and Bioengineering*, 2008, **100**, 579-586.

14. Y. S. Shin, K. Cho, J. K. Kim, S. H. Lim, C. H. Park, K. B. Lee, Y. Park, C. Chung, D. C. Han and J. K. Chang, *Analytical Chemistry*, 2004, **76**, 7045 - 7052.

15. Y. Huang and B. Rubinsky, *Sensors and Actuators A*, 2001, **89**, 242-249.

16. M. Khine, C. Ionescu-Zanetti, A. Blatz, L. Wang and L. P. Lee, *Lab on a Chip*, 2007, **7**, 457-462.

17. A. Valero, J. N. Post, J. W. van Nieuwkasteele, P. M. ter Braak, W. Kruijer and A. van den Berg, *Lab on a Chip*, 2008, **8**, 62-67.

18. S. Wang, X. Zhang, W. Wang and L. J. Lee, *Analytical Chemistry* 2009 **81**, 4414-4421.

19. E. G. Guignet and T. Meyer, *Nature Methods*, 2008, **5**, 393-395.

20. Y. Zhan, J. Wang, N. Bao and C. Lu, *Analytical Chemistry*, 2009, **81**, 2027-2031.

21. M. Li, Y. C. Lin, K. C. Su, M. I. Liao and C. S. Yeh, *7th International Conference on Miniaturized Chemical and Biochemical Analysis Systems* 2003, 661-664.

22. V. G. Zarnitsyn and M. R. Prausnitz, *Ultrasound in Medicine & Biology*, 2004, **30**, 527 - 538.

23. H. D. Liang, J. Tang and M. Halliwell, *Proceedings of the Institute of Mechanical Engineers*, 2009, **224**, 343-361.

24. S. Bao, B. D. Thrall and D. L. Miller, *Ultrasound in Medicine & Biology*, 1997, **23**, 953 - 959.

25. M. Kinoshita and K. Hynynen, *Biochemical and Biophysical Research Communications*, 2007, **359**, 860-865.

26. H. R. Guzman, D. X. Nguyen, S. Khan and M. R. Prausnitz, *Journal of Acoustical Society of America*, 2001, **110**, 588-596.

27. J. Liu, T. N. Lewis and M. R. Prausnitz, *Pharmaceutical Research*, 1998, **15**, 918-924.

28. Y. Taniyama, K. Tachibana, K. Hiraoka, M. Aoki, S. Yamamoto, K. Matsumoto, T. Nakamura, T. Ogihara, Y. Kaneda and R. Morishita, *Gene Therapy*, 2002, **9**, 372-380.

29. S. Koch, P. Pohl, U. Cobet and N. Rainov, *Ultrasound in Medicine & Biology*, 2000, **26**, 897-903.

30. R. K. Schlicher, H. Radhakrishna, T. P. Tolentino, R. P. Apkarian, V. G. Zarnitsyn and M. R. Prausnitz, *Ultrasound in Medicine & Biology*, 2006, **32**, 915-924.

31. C. X. Deng, F. Sieling, H. Pan and J. Cui, *Ultrasound in Medicine & Biology*, 2004, **30**, 519-526.

32. T. Siu, D. M. Trivedi, M. Chiao and R. Rohling, *The 13th International Conference on Solid-State Sensors, Actuators and Microsystems*, Seoul, 2005, 205-208.

33. T. C. Marentis, B. Kusler, G. G. Yaralioglu, S. Liu, E. O. Haeggstrom and B. T. Khuri-Yakub, *Ultrasound in Medicine & Biology*, 2005, **31**, 1265-1277.

34. Y. Yamashita, M. Shimada, K. Tachibana, N. Harimoto, E. Tsujita, K. Shirabe, J. Miyazaki and K. Sugimachi, *Human Gene Therapy*, 2002, **13**, 2079-2084.

35. J. M. Escoffre, K. Kaddur, M. P. Rols and A. Bouakaz, *Ultrasound in Medicine & Biology*, 2010, **36**, 1746-1755.

36. H. Becker and L. E. Locascio, *Talanta*, 2002, **56**, 267 - 287.

37. C. G. K. Malek, *Analytical & Bioanalytical Chemistry*, 2006, **385**, 1362 - 1369.

38. J. Y. Cheng, C. W. Wei, K. H. Hsu and T. H. Young, *Sensors and Actuators B*, 2004, **99**, 186 - 196.

39. W. Pfleging and O. Baldus, *Proceedings of SPIE*, 2006, **6107**, 1-12.

40. H. Klank, J. P. Kutter and O. Geschke, *Lab on a Chip*, 2002, **2**, 242 - 246.

41. D. Snakenborg, H. Klank and J. P. Kutter, *Journal of Micromechanics and Microengineering*, 2004, **14**, 182 - 189.

42. M. F. Jensen, M. Noerholm, L. H. Christensen and O. Geschke, *Lab on a Chip*, 2003, **3**, 302 - 307.

43. D. Yuan and S. Das, *Journal of Applied Physics*, 2007, **101**, 1-6.

44. S. C. Wang, C. Y. Lee and H. P. Chen, *Journal of Chromatography A*, 2006, **1111**, 252 - 257.

45. N. C. Nayak, Y. C. Lam, C. Y. Yue and A. T. Sinha, *Journal of Micromechanics and Microengineering*, 2008, **18**, 1-7.

46. C. K. Chung, Y. C. Lin and G. R. Huang, *Journal of Micromechanics and Microengineering*, 2005, **15**, 1878 - 1884.

47. H. Qi, X. Wang, T. Chen, X. Ma and T. Zuo, *Microsystem Technologies*, 2009, **15**, 1027 - 1030.

48. D. Lim, E. G. Santoso, K. M. Teh, S. Wan and H. Y. Zheng, *Surface Review and Letters*, 2006, **13**, 795 - 802.

49. G. Villanueva, O. Vazquez-Mena, C. Hibert and J. Brugger, *22nd IEEE International Conference on MEMS*, Sorrento, 2009, 144 - 147.

50. S. W. Pang, M. W. Geis, W. D. Goodhue, N. N. Efremow, D. J. Ehrlich, R. B. Goodman and J. N. Randall, *Journal of Vacuum Science and Technology*, 1988, **6**, 249 - 252.

51. T. Shibata, K. Suguro, K. Sugihara, T. Nishihashi, J. Fujiyama and Y. Sakurada, *IEEE Transactions on Semiconductor Manufacturing*, 2002, **15**, 183 - 188.

52. M. Graff, S. K. Mohanty, E. Moss and A. B. Frazier, *Journal of Microelectromechanical Systems*, 2004, **13**, 956 - 962.

53. A. Holke and H. T. Henderson, *Journal of Micromechanics and Microengineering*, 1999, **9**, 51-57.

54. F. S. S. Chien, W. F. Hsieh, S. Gwo, A. E. Vladar and J. A. Dagata, *Journal of Applied Physics*, 2002, **91**, 10045-10050.

55. G. Yan, P. C. H. Chan, I. M. Hsing, R. K. Sharma, J. K. O. Sin and Y. Wang, *Sensors and Actuators A*, 2001, **89**, 135-141.

56. H. Qi, T. Chen, L. Yao and T. Zuo, *Optics and Lasers in Engineering*, 2009, **47**, 594 - 598.

57. N. Y. Lee and B. H. Chung, *Langmuir*, 2009, **25**, 3861-3866.

58. W. G. Lee, H. Bang, H. Yun, J. Min, C. Chung, J. K. Chang and D. C. Han, *Lab on a Chip*, 2008, **8**, 224-226.

59. S. Rodamporn, S. P. Beeby, N. R. Harris, A. D. Brown and J. E. Chad, *Proceedings of ThaiBME*, 2007, 234-238.

60. J. K. Valley, S. Neale, H. Y. Hsu, A. T. Ohta, A. Jamshidi and M. C. Wu, *Lab on a Chip*, 2009, **9**, 1714-1720.

61. D. A. Christensen, *Ultrasonic Bioinstrumentation*, John Wiley and Sons, 1988.

62. X. Zhuang, D. S. Lin, O. Oralkan and B. T. Khuri-Yakub, *Journal of Microelectromechanical Systems*, 2008, **17**, 446-452.

63. J. A. Kim, K. Cho, M. S. Shin, W. G. Lee, N. Jung, C. Chung and J. K. Chang, *Biosensors and Bioelectronics*, 2008, **23**, 1353-1360.

64. J. Glahder, B. Norrild, M. B. Persson and B. R. R. Persson, *Biotechnology and Bioengineering*, 2005, **92**, 267-276.

65. H. He, D. C. Chang and Y. K. Lee, *Bioelectrochemistry*, 2007, **70**, 363-368.

66. C. Y. Lai, C. H. Wu, C. C. Chen and P. C. Li, *Ultrasound in Medicine & Biology*, 2006, **32**, 1931-1941.

67. J. Feril, L.B., R. Ogawa, K. Tachibana and T. Kondo, *Cancer Science*, 2006, **97**, 1111-1114.

68. W. S. Chen, X. Lu, Y. Liu and P. Zhong, *Journal of Acoustical Society of America*, 2004, **116**, 2440-2450.

69. S. Rodamporn, N. R. Harris, S. P. Beeby, R. J. Boltryk and T. Sanchez-Elsner, *IEEE Transactions on Biomedical Engineering*, 2011, **58**, 927-934.

VITA

Name: Whitney Leigh Longsine

Address: Texas A&M University
c/o Dr. Arum Han
Department of Electrical and Computer Engineering
College Station, TX 77843-3128

Email Address: wlongsine@gmail.com

Education: B.S., Electrical Engineering, Texas A&M University, 2007
M.S., Electrical Engineering, Texas A&M University, 2011